

# Enabling photodetection electronics for fluorescent diamond based quantum sensing

Vladislav Serafimov

December 19, 2025

# Contents

<b>1 Foreword</b>	<b>3</b>
<b>2 Summary</b>	<b>4</b>
<b>3 Introduction</b>	<b>5</b>
3.1 Background . . . . .	5
3.2 Purpose of the assignment . . . . .	5
3.3 Assignment specifications . . . . .	6
3.4 Scope of work . . . . .	6
3.4.1 Project boundaries . . . . .	6
3.4.2 Goals . . . . .	7
3.4.3 Deliverables . . . . .	8
3.5 Methodology . . . . .	8
3.6 Report outline . . . . .	8
<b>4 Functional design</b>	<b>10</b>
4.1 Background knowledge . . . . .	10
4.1.1 Spin states . . . . .	10
4.1.2 Zeeman effect . . . . .	10
4.1.3 Energy levels . . . . .	10
4.2 Quantum protocols . . . . .	11
4.2.1 CW-ODMR . . . . .	11
4.2.2 $T_1$ relaxometry . . . . .	12
4.2.3 P-ODMR . . . . .	13
4.3 Quantum sensing setup . . . . .	13
4.4 Laser driver . . . . .	14
4.5 Photodetection . . . . .	14
4.5.1 Photodiodes . . . . .	14
4.5.2 TIA design . . . . .	15
4.5.3 Power requirements . . . . .	15
4.6 Lock-in amplification . . . . .	17
<b>5 Technical design</b>	<b>18</b>
5.1 Current driver . . . . .	18
5.1.1 Pulsing sequences . . . . .	18
5.2 Photodetector design . . . . .	19
5.2.1 First iteration . . . . .	19
5.2.2 Second iteration . . . . .	19
5.2.3 Third iteration . . . . .	22
5.2.4 Fourth iteration . . . . .	23
5.3 Photodetection simulation . . . . .	25
5.3.1 First iteration . . . . .	25
5.3.2 Second iteration . . . . .	26
5.3.3 Third iteration . . . . .	27
5.3.4 Fourth iteration . . . . .	27
5.4 Photodetection implementation . . . . .	29
5.4.1 First iteration . . . . .	29
5.4.2 Second iteration . . . . .	29
5.4.3 Third iteration . . . . .	29

<b>6 Testing and results</b>	<b>31</b>
6.1 Test goals . . . . .	31
6.2 Test setup . . . . .	32
6.2.1 Photodiode-model characterization . . . . .	32
6.2.2 S-parameter characterization . . . . .	32
6.2.3 Integration test . . . . .	32
6.3 Results . . . . .	33
6.3.1 Photodiode-model characterization . . . . .	33
6.3.2 S-parameter characterization . . . . .	33
6.3.3 TIA integration test . . . . .	33
6.4 Discussion . . . . .	34
6.5 Known limitations . . . . .	34
<b>7 Conclusion</b>	<b>35</b>
<b>8 Recommendations</b>	<b>36</b>
<b>Appendices</b>	<b>37</b>
<b>A Code</b>	<b>37</b>
<b>Glossary</b>	<b>41</b>

# Chapter 1

## Foreword

## Chapter 2

# Summary

Quantum sensing is a developing technology with numerous applications in the real world. At present, there is a need for smaller and cheaper quantum sensors. The Applied Nanotechnology research group is one of the many organizations working on a setup with these criteria in mind. However, quantum sensing protocols do not use conventional electrical circuits for measurements, but instead use and manipulate light. Purely optical designs are not possible, which is why the light from the quantum setup needs to be translated to electrical signals. For this project, the student was tasked with solving the challenge of detecting low-intensity light by creating a compact and affordable photodetector. Furthermore, the integration of the different subsystems of the quantum sensing setup needed to be worked on. Using a methodological approach, in the form of the V-Model, the project was tackled and completed successfully. A working photodetector was built to be used for magnetic field measurements using one of the fundamental quantum sensing protocols, **Constant-Wave ODMR (ODMR)**. Even though other protocols are not supported by the current version of the detector, due to their high bandwidth requirements, further development can enable the setup to measure pulsed protocols at high frequencies. Additionally, higher sensitivity can be achieved by switching the p-i-n photodiode for an avalanche photodiode, although it is going to significantly increase the cost of the sensing setup.

# Chapter 3

## Introduction

This chapter introduces the assignment, along with some foundational concepts of quantum sensing. Furthermore, it covers the methodology, goals and boundaries, which all help outline the trajectory of the project.

### 3.1 Background

Nitrogen Vacancy (NV) centers [1] are imperfections in the atomic structure of diamonds. The two types of NV centers are NV<sup>0</sup> and NV<sup>-</sup>, as seen in Figure 3.1, but the NV<sup>-</sup> structure is much more commonly used in quantum applications. These imperfections have the useful property of spin-dependent luminescence. This means that the spin of the NV center affects the frequency of the light emitted by the structure<sup>1</sup>. Using this quality of the NV structure, different environmental metrics (e.g magnetic fields) can be measured.

The Applied Nanotechnology research group is working on a NV-center-based sensor setup. There exist several quantum protocols, but the one this setup needs to support is called CW-ODMR. At its core, Optically Detected Magnetic Resonance (ODMR) is a set of protocols, which can detect magnetic fields based on the fluctuations in the fluorescence of NV centers [3]. CW-ODMR in particular involves exposing the NV center to a Microwave (MW) sweep while illuminating it with a constant light source. This is in contrast with Pulsed ODMR (ODMR) techniques, which use different Transistor-Transistor Logic (TTL) pulse schemes [4] to modulate the MW signal and the light source.

Acquiring and processing data from the setup requires working with weak signals that are hard to distinguish from the environmental noise. While this is a significant problem, it is also very common. Because of this, the industry has already adopted systems to detect weak light sources and measure their intensity. This project is mainly about developing a similar photodetection system for the NV setup.

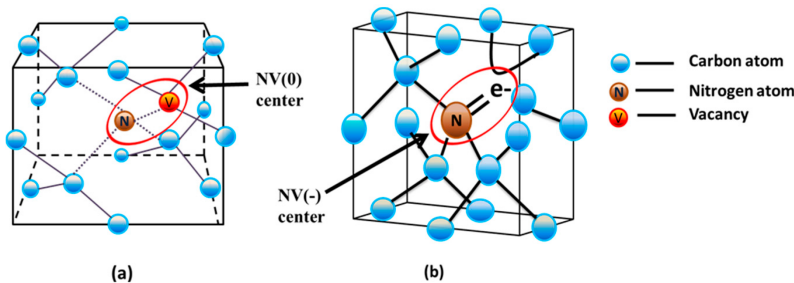


Figure 3.1: NV<sup>0</sup> (a) and NV<sup>-</sup> (b) structures in diamonds (image credit to Haque et al [5])

### 3.2 Purpose of the assignment

The main purpose of the assignment is to implement a photodetector. The quantum sensing setup requires is made up of other systems as well, which is why there are also several additional functionalities and systems that need to be developed.

<sup>1</sup>The NV center only emits light after absorbing photons, a phenomenon called photoluminescence [2]

Firstly, a custom photodetector needs to be designed. The circuit should accommodate the sensors and output to a lock-in amplifier. After establishing connection, an **Open Lock-In Amplifier (OLIA)**<sup>2</sup> circuit needs to be tested and compared to conventional lock-in systems. Additionally, a control interface can be implemented, if there is enough time. It needs to be programmed so that it can control all necessary features of the lock-in amplifier. Aside from the data acquisition system, work also needs to be done on the existing laser-driver, as it needs to be tested and the pulsing sequences for it need to be programmed.

### 3.3 Assignment specifications

As already explained, the assignment is quite broad and involves both hardware and software, causing the need for a number of different tools.

Most of the hardware tools are already available at the Applied Nanotechnology lab. The lock-in amplifiers which will be used for the tests are the most important pieces of hardware. Zurich Instruments HF2LI is the benchmark lock-in amplifier. The target amplification is at least 10dB. Chapter 3.1 already discussed the basics of the **CW-ODMR** protocol. In order to get an operational **CW-ODMR** setup, an **MW** generator and a laser will be used. **MW** sweeping needs to be done in the range of 2,8 to 2,9 GHz and the lab already has a custom-built **MW** generator that can output these frequencies. The laser is mostly outside the scope of the assignment, as it is almost entirely optical in nature. The driving circuitry for it has been developed by a previous intern, but the integration with the sensing setup will be carried out in this project. The driver will be fed **TTL** pulse data from an Analog Discovery 2. It is important to note that the fluorescence wavelength is in the range of 637 to 800 nm, as it plays an important part in photodetection. It is different from the laser wavelength, which is filtered out and is not supposed to be detected by the photodetector.

In terms of software, there is more freedom of choice. Interfacing with the HF2LI is done through proprietary software. Similarly, pulse generation is going to be done with Waveforms, the Analog Discovery 2 software, but those are the only programs that cannot be replaced. As for **Electronic Computer-Aided Design (ECAD)** software, there are various suites that offer the same base functionality. KiCad was selected because the client prefers open-source software. The program for retrieving data from the lock-in amplifiers can be written in both Python and MATLAB. Both languages have good integration with the main lock-in amplifier. They also offer **Graphical User Interface (GUI)** programming capabilities and are good for scientific computing overall.

### 3.4 Scope of work

The scope of the project was extensively discussed with the company coach. Chapter 3.4.1 sets the scope and Chapter 3.4.2 builds on it, providing more specific details.

#### 3.4.1 Project boundaries

The project boundaries were initially based on the assignment form, but were later discussed with the client and refined further.

##### Must have

- Hardware platform for photodetection
- Software for signal processing and visualization
- Setup integration

##### Should have

- Tests with different quantum protocols
- Tests with different diamond samples

##### Could have

- **OLIA** implementation
- Tests comparing **OLIA** to market solutions

---

<sup>2</sup>**OLIA** is an open-source microcontroller-based lock-in amplifier. It uses common components, which makes it easy to build [6]

### Will not have

- Laser as a part of the hardware platform
- Laser driver upgrade

#### 3.4.2 Goals

Based on the MoSCoW priorities from Chapter 3.4.1, a set of goals was created to further specify all items from each prioritization category. Every goal was designed so that its outcome results in a tangible project milestone (e.g. a deliverable).

Goal 1 : Create a hardware setup, which measures and amplifies photodiode signals

Goal 2 : Develop software to drive the laser and process lock-in amplifier signals

Goal 3 : Compare the performance of different lock-in amplifiers

While these goals are practical, they are still not specific enough. To eliminate the possibility of confusion, a set of tasks were created. All tasks contribute to one of the three goals.

Task 1.1 : Design a photodetector **Printed Circuit Board (PCB)**

Task 1.2 : Build an operable **OLIA**

Task 1.3 : Set up and test laser driver

Task 2.1 : Develop software that acquires signals and is then able to visualize them

Task 2.2 : Program quantum protocol pulse sequences for the laser driver

Task 3.1 : Use key performance metrics to compare the **OLIA** implementation to market solutions

Task 3.2 : Measure test setup performance using different diamond samples and quantum protocols

**Task 1.1** involves the design and production of a photodiode **PCB**. The **PCB** has to output signals that are not only compatible with lock-in amplifiers that are available on the market, but also with the **OLIA**. This part of the hardware design has the highest priority, which is why it will be done first.

**Task 1.2** is to build an **OLIA** amplifier, which can be used at Applied Nanotechnology's laboratory. This will be done with the technical specifications and firmware provided by Harvie and de Mello [6]. The necessity for an **OLIA** is low, because the Applied Nanotechnology research group already has two lock-in amplifiers.

**Task 1.3** is one of the more minor hardware tasks. As the driver is already designed and fabricated, it only needs to be tested and integrated with the rest of the setup. Tests should show that the driver can switch the laser at high speeds, which is necessary for several quantum protocols.

**Task 2.1** is to write an application in Python or MATLAB. This can be done on a different setup, but ideally it will use the hardware setup from **Goal 1**. Because the **OLIA** project uses open-source firmware that differs from proprietary solutions, there might need to be two separate applications. This task can only be completed once a measurement setup is built, so its execution will follow the first two tasks.

**Task 2.2** makes sense only as a continuation of **Task 1.3**. Proper integration testing requires pulsing sequences, which will also be used when the setup is functional. These sequences are vital for the second stage of testing of the laser driver, so they need to be developed while the driver is still being tested with simple periodic signals.

**Task 3.1** requires all previous tasks to be finished. The completed setup needs to be used to measure the performance of lock-in amplifiers available on the market and the **OLIA** implementation. **Signal-to-Noise Ratio (SNR)**, bandwidth and stability are the main metrics that need to be compared.

**Task 3.2** is similar to **Task 3.1**, but it is a much broader in scope. Using different diamond samples and quantum protocols will show how the sensing setup performs and how different conditions affect it. Because the task can be used to verify the photodetector from **Goal 1**, it can also be done before **Task 3.1**. Tests with varying diamond samples are more important to the client, which is why they will take precedence over tests with different quantum protocols.

### 3.4.3 Deliverables

The description of the tasks already provided context for the deliverables, but this subsection contains a formalized version of the deliverables.

1. Photodetection PCB
2. OLIA implementation
3. Data acquisition application
4. Pulsing sequences
5. Technical documentation

The only deliverable, which was not mentioned in Chapter 3.4.2 is the technical documentation. This is because it should contain information about every task.

## 3.5 Methodology

The V-Model methodology was selected, as it is well-suited for low-level projects. Figure 3.2 shows a diagram of the phases of the V-Model. Unlike some software-oriented models, the V-Model is very sequential. This can sometimes be seen as detrimental, but in this case it helps with structuring the project. Another benefit of this model is that there are multiple testing activities, which underpin the quality assurance. A contentious feature of the V-Model is the heavy reliance on the initial requirements. This need for deliberate project requirements can be hard to meet, especially if the client representative is not technically proficient. However, this is not the case in this project. The requirements were extensively discussed with the client representative, based on which the project boundaries in Chapter 3.4.1 were set up.

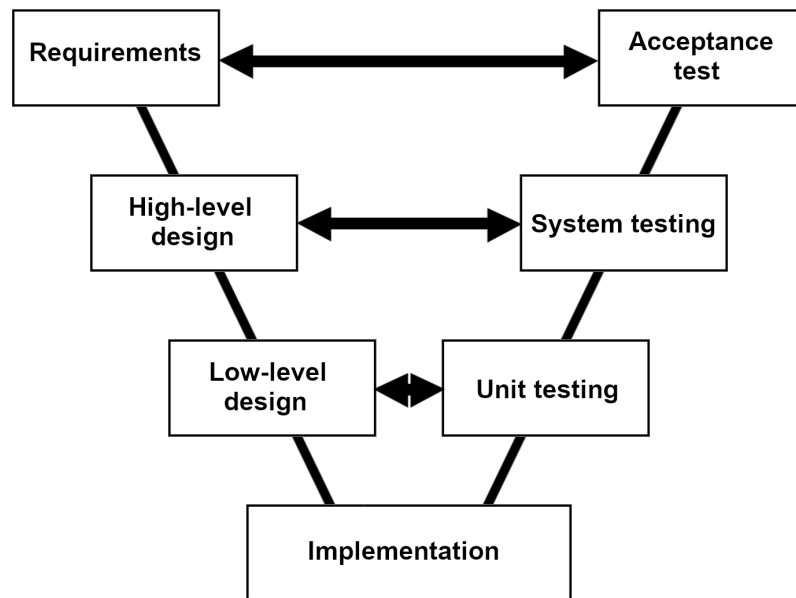


Figure 3.2: V-Model diagram

## 3.6 Report outline

The introduction is followed by the functional design chapter, which introduces background knowledge, needed to understand the NV setup. After that, the high-level design of the system is presented. It explains the functionality of the various systems that make up the project without delving into specifics.

After that, the technical design explores the low-level design of the systems of the project. It mentions all the necessary details, including calculations, simulations and implementation steps.

Following the design sections, the testing chapter describes the testing goals and what methods were used for measuring. The chapter then presents the test results.

Lastly, the conclusion and recommendation chapters summarize the outcomes of the project and offer proposals for further development.

# Chapter 4

## Functional design

The functional design presents a high-level overview of the project and what explains what design choices were made on a system-level. Additionally, it provides tangential information that can be useful for understanding the working principle of the quantum sensing setup.

### 4.1 Background knowledge

Some background knowledge is required to understand the purpose of the projects, because the setup the project revolves around uses several non-trivial physics concepts. This section outlines the basic ideas behind the physics that enable the quantum sensing setup to work.

#### 4.1.1 Spin states

Spin, at least in quantum mechanics, is the intrinsic angular momentum of a particle, which is described by the quantum number of the particle. Importantly, it differs from the angular momentum in classical mechanics, which is extrinsic. Spin characterizes systems of particles, usually electrons, using quantum entanglement. This phenomenon refers to the "entanglement", or spin correlation, of a set of particles.

These foundational concepts make it possible to describe quantum systems using various states. The most simple states, used as descriptors, are the energy states. Ground states refer to the system being in an energy minimum. On the other hand, excited states signify that the system has more energy than at its ground state. Additionally, there can be intermediate states during state transition.

While the aforementioned states describe system energy, they have no bearing on the spin. For the purposes of this project, only two spin states need to be explained. The first one is called singlet state. It occurs when an entangled system has a total spin of 0, caused by the mutual cancellation of spin. For example, for a system of two entangled electrons to be a singlet, the two spins would need to point in opposite directions. The second spin state is called triplet and it has a total spin of 1. Triplets can consist of, for instance, two unpaired electrons with aligned spins that sum up to 1. Singlets and triplets both have major distinguishing features and properties, which is why they can be used for quantum sensing. Aside from the difference in spin, triplets tend to have higher energy levels. They also exhibit attraction to magnetic fields, while singlets cannot be influenced directly by magnetism.

#### 4.1.2 Zeeman effect

Discovered by Pieter Zeeman in 1896, the Zeeman effect is another important phenomenon that enables quantum sensing. If under normal circumstances a light-emitting quantum system only emits one spectral line, then when a magnetic field is applied to it the line will split, thus exhibiting the Zeeman effect. In an NV center, this phenomenon causes the  $|\pm 1\rangle$  energy level to split into  $|+1\rangle$  and  $| -1\rangle$ .

#### 4.1.3 Energy levels

Figure 4.1 shows the energy level diagram of an NV center.

After illuminating the NV center with a green laser, electrons go from a ground state to an excited state. They then need to return to the ground state. This decay process is usually direct

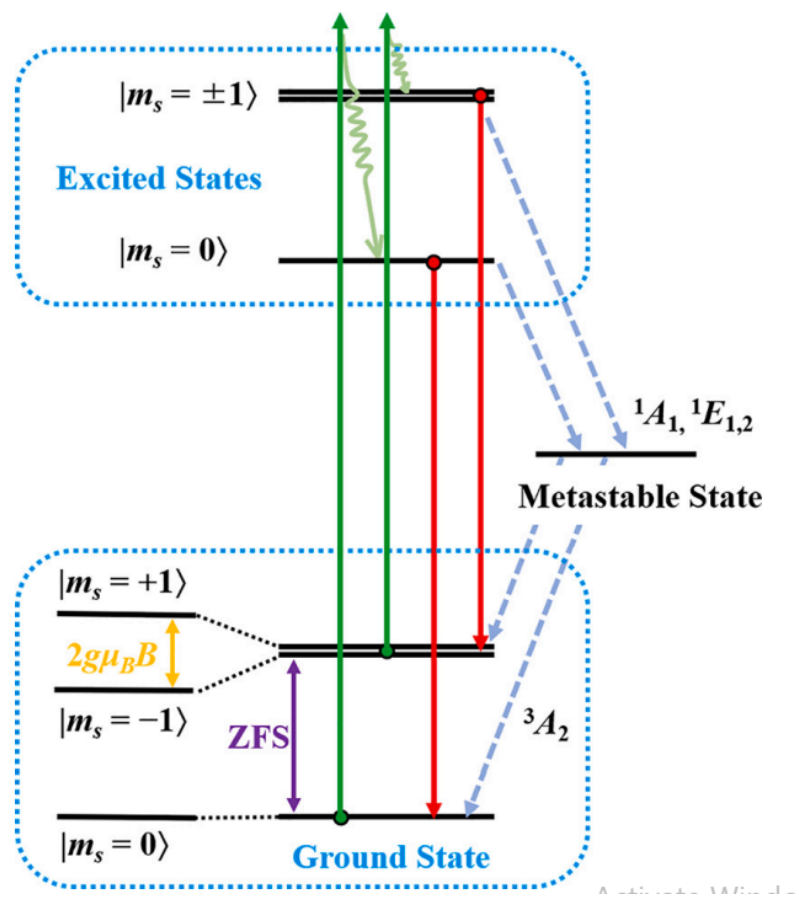


Figure 4.1: NV center energy level diagram (image credit to Song et al [7])

and emits a red photon, however it can also go through the metastable singlet state and emit an infrared photon. It should be noted that whenever the NV center is exposed to the resonant frequency  $\nu = 2,87\text{GHz}$  the probability of emitting an infrared photon is significantly increased.

## 4.2 Quantum protocols

There are a number of different quantum protocols, which differ in what they can measure, in how precisely they can measure it and in the complexity of the hardware they require to operate. **CW-ODMR** is the main protocol this project is aimed at facilitating. As Saijo et al [8] demonstrate, **CW-ODMR** is relatively simple, while still detecting magnetic field with reasonable sensitivity. **P-ODMR** does outperform **CW-ODMR** [9], but because of the added complexity working with it is a "Could have" (see Chapter ??). Before being able to run **P-ODMR** on the setup at the lab, several protocols need to be implemented first [4].  $T_1$  measurements, which are one of the fundamentals of **Magnetic Resonance Imaging (MRI)**, should be conducted first. Afterwards, Rabi oscillations need to be observed and measured in order to calibrate the setup. Without these intermediate protocols, **P-ODMR** cannot be performed.

### 4.2.1 CW-ODMR

**CW-ODMR** is a quantum protocol that has seen extensive usage in sensing setups that measure magnetic fields. Its working principle is centered around the photoluminescence of NV centers and the difference in light emission based on spin states. As already discussed in Chapter 4.1.3, the NV center emits less visible light when at the resonant frequency  $\nu$ . Additionally, two more dips appear on the spectrum if a magnetic field is applied. Calculating the magnetic field can be done using the formula  $h\nu = g_e\mu_B B_{AC}$ <sup>1</sup>. Figure 4.2 shows an example of what a **CW-ODMR** spectrum might look like.

<sup>1</sup>3, In the formula,  $h$  is the Planck constant,  $g_e$  is the g-factor of the electron and  $\mu_B$  is the Bohr magneton. Knowing all other variables,  $B_{AC}$  can easily be calculated.

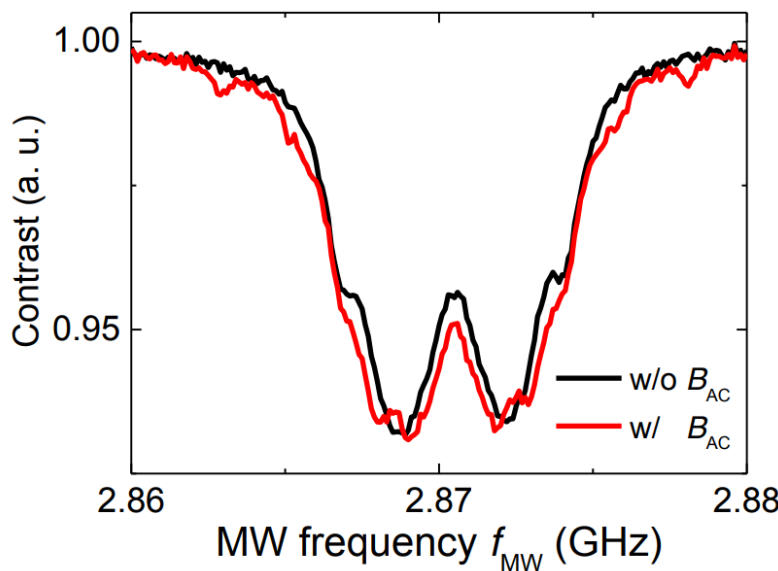


Figure 4.2: Example of a CW-ODMR spectrum **with** and **without** a magnetic field (image credit Saijo et al [8])

#### 4.2.2 $T_1$ relaxometry

$T_1$ ,  $T_2$  and  $T_2^*$  relaxation time measurements are commonly associated with radiometry [10], but they have other uses too.  $T_1$  measurements, in particular, are useful in the realm of quantum sensing. Knowing the  $T_1$  relaxation time, which refers to the time it takes for the spins in an NV system to decay back to their original state, makes it possible to adjust the pulse sequences of more complex protocols and thus get better results.

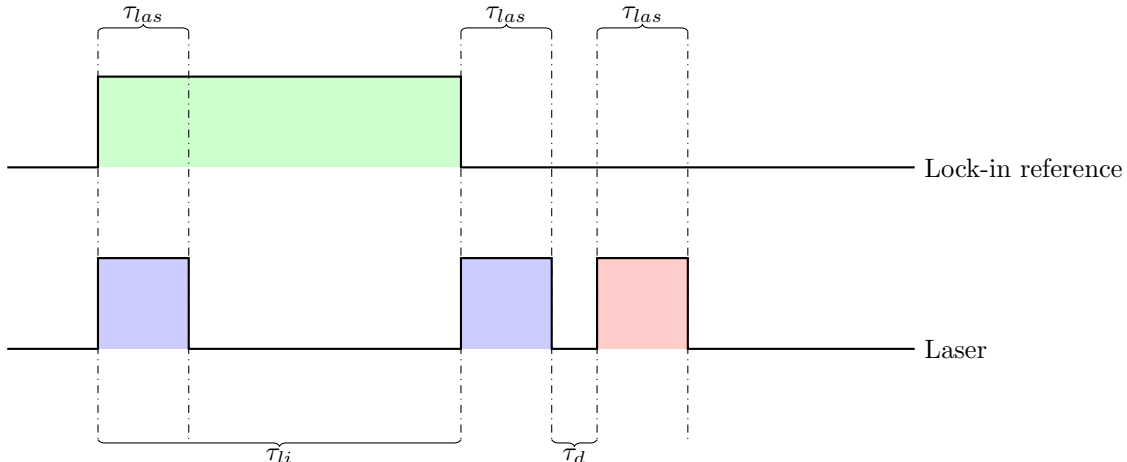


Figure 4.3: Laser and reference signals for  $T_1$  measurements

The waveforms which are needed for  $T_1$  measurements are shown in Figure 4.3. While both are important in practice, the lock-in is not as relevant, at least in this section of the report. However, its working principle is explored in Chapter 4.6. For now, all that needs to be said about the lock-in reference signal is that it is periodic and  $\tau_{li}$  is much longer than  $\tau_{las}$  (Sewani et al [4] propose  $\tau_{li} = 15ms$  and  $\tau_{las} = 5\mu s$ ). Laser pulses, on the other hand, are not periodic. Instead, there are three short pulses every reference period (which is  $2\tau_{li}s$  long). The two blue pulses have the same timing every cycle, because they initialize the NV spins. However, the red pulse always occurs after the variable dark time  $\tau_d$ . Depending on the  $T_1$  decay at the time of the readout pulse, a different voltage will be detected. Figure 4.4 shows what results can be expected when measuring  $T_1$ . Determining the value of  $T_1$  is done using Formula 4.1, where  $I$  is the light intensity,  $I_\infty$  is the light intensity offset and  $\tau_d$  is the dark time.

$$I(t) = I_\infty + I(0)e^{-\tau_d/T_1} \quad (4.1)$$

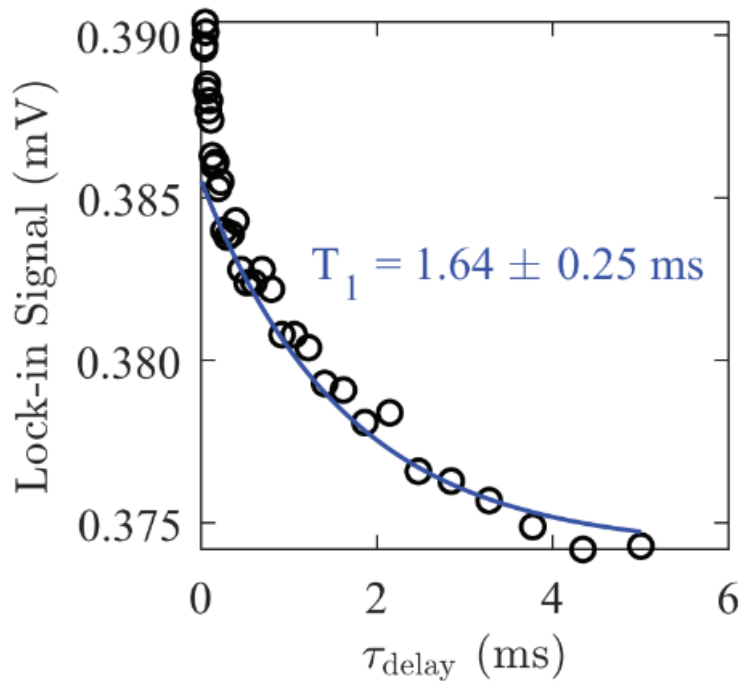


Figure 4.4: Results of a set of  $T_1$  measurements with varied dark time  $\tau_d$  (image credit to Sewani et al [4])

#### 4.2.3 P-ODMR

As a descriptor **P-ODMR** is somewhat vague, which is why it has been used for a number of protocols. Different pulse schemes can result in radically different . Some researches use

### 4.3 Quantum sensing setup

Executing all of the aforementioned protocols requires a sensing setup with some specific capabilities. This section discusses the devices that make up the setup and the functionalities required by each protocol.

A high-level diagram of the quantum sensing system can be seen in Figure 4.5. There are 2 input devices in the system, but most protocols exclusively use the function generator. On the other hand, only a single lock-in amplifier is used as an output device for all measurements.

The blue boxes show the components responsible for sending and receiving light signals. They constitute the core of the setup. Waveforms are generated by the function generator, no matter the protocol. Using a current driver, the laser is then used to illuminate the diamond sample. The resulting luminescence is then measured by the photodetector and processed by the lock-in amplifier. All protocols need this part of the setup, however they utilize it differently.

Microwave generation, when needed, starts with a **TTL** signal from the function generator or a frequency sweep using a dedicated device. Out of all protocols, only **CW-ODMR** requires a sweep. The antenna then broadcasts the signal, while the switch isolates the signal generator from it.

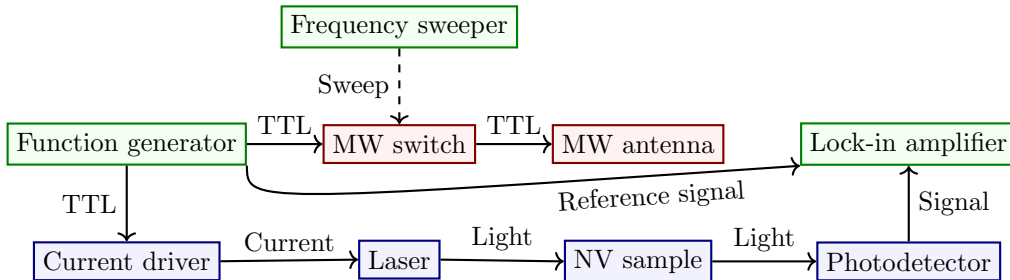


Figure 4.5: High-level overview of the quantum sensing setup

## 4.4 Laser driver

As discussed in Chapter 3.3, the laser driver has already been designed and built. It gets **TTL** signals from a waveform generator and outputs current to drive the connected laser.

However, the designer explicitly states that tests were only done with frequencies of up to 100 kHz [11]. This is insufficient for the project, as for example, the pulsing sequence for  $T_1$  measurements use pulses with duration of 5  $\mu\text{s}$  and downtime of as little as 1  $\mu\text{s}$ <sup>2</sup>.

## 4.5 Photodetection

Photodetection is how the **NV** photoluminescence is measured, effectively turning light into current using a photodiode. However, a bare photodiode cannot be connected to a lock-in amplifier, because it functions as a current generator. This is where the photodetection **PCB** comes in. Its purpose is to transform the current into voltage and then amplify the resulting signal to the necessary voltage level.

### 4.5.1 Photodiodes

At the heart of the photodetector lies the photodiode. It is what turns light into current and drives the **Transimpedance Amplifier (TIA)** that follows it. While the specifications of the diode are not the most important part of the photodetector circuit, they still need to be discussed, due to the impact the two ways of biasing can have on the circuit.

The two most common photodiode are shown in Figure 4.6. Reverse-biased circuits, similar to the one in Figure 4.6a, are used in optical receivers and other high-speed use cases. However, the drawback of biasing the diode using the negative supply voltage  $V_{EE}$  is that it results in an increased dark current, which is current that, unlike photocurrent, runs through the diode without any light being present. Precise low-light measurements, such as those needed by the quantum setup, require the photodetector to have high linearity, which cannot be achieved when the dark current is comparable to the photocurrent. Photovoltaic-mode biasing reduces the dark current at the cost of signal strength and bandwidth [12]. This configuration is much more common in low-illumination setups, where the signals can be in the nanoampere to picoampere range. As the photoluminescent **NV** centers emit extremely low amounts of light, the photovoltaic configuration was chosen for the photodetector implementation for the quantum sensing setup.

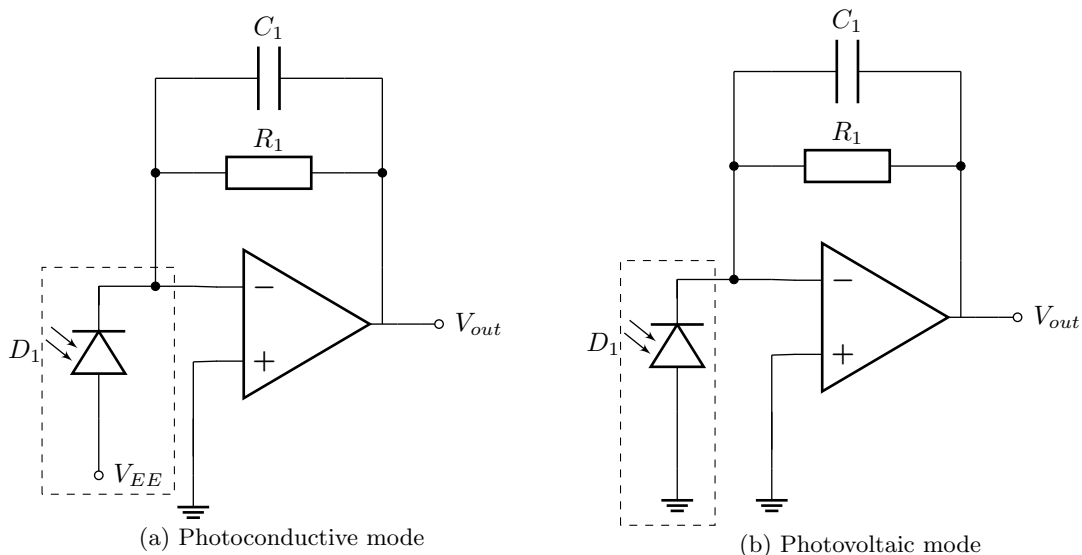


Figure 4.6: Reverse-bias photodiode configurations

<sup>2</sup>These values are taken from Sewani et al [4], but the clients wants to make the timings used by the quantum sensing setup even faster

#### 4.5.2 TIA design

Designing the photodetector is mostly about creating a **TIA**, which is a tool used for converting current to voltage, and specifically tuning its parameters so that it works with the selected photodiode under operating conditions.

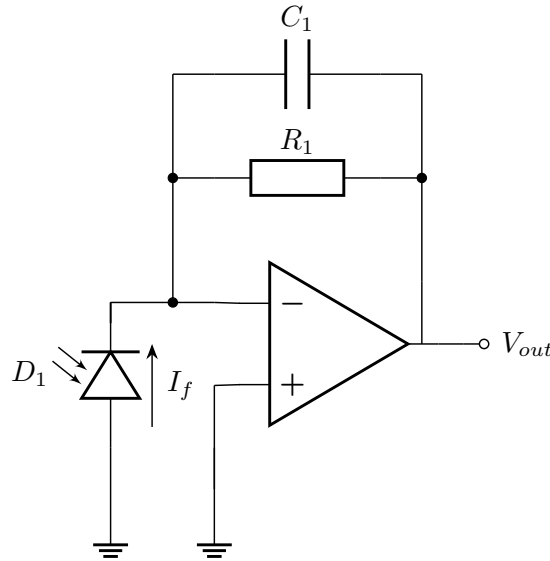


Figure 4.7: Basic **TIA** circuit

The basic circuit, shown in Figure 4.7, is all that is required for photodetection. Following the Texas Instruments guidelines for making a **TIA** [13], all the parameters of the circuit can be calculated.

$$R_1 = \frac{V_{o\ max}}{I_{f\ max}} \text{ assuming } V_{o\ min} = 0V \quad (4.2)$$

The resistor  $R_1$  determines the transimpedance gain of the amplifier. Equation (4.2) shows how its value can be calculated by using the output voltage and input current. It should be noted that the minimum output voltage is always 0 in this use case.

$$C_1 = \frac{1}{2\pi R_1 f_{rc}} \quad (4.3)$$

The capacitance of  $C_1$  can be calculated using the resistance of  $R_1$  and the cutoff frequency  $f_{rc}$ , as shown in Equation (4.3).

In addition, a non-inverting amplifier can be added, to increase the gain of the circuit even more, without affecting the phase. Figure 4.8 shows how it can be connected to the output of the **TIA** from Figure 4.7.

Equation (4.4) is used to calculate the gain of second amplification stage. The formula is derived from the voltage divider formed by the two resistors and the fact that  $V_{ot} = V_-$ .

$$A_{nia} = \frac{V_{out}}{V_{ot}} = 1 + \frac{R_3}{R_2} \quad (4.4)$$

The design is based on circuits provided by the client. At their request, the first version of the PCB is an exact replica of the original circuit.

#### 4.5.3 Power requirements

Knowing the power needs of the photodetector is important for decreasing the size of the quantum setup. As bench power supplies take up a lot of space and exceed the photodetector requirements by orders of magnitude, an on-board supply or a breakout board will better fit the project. To minimize overhead while still having a supply that can handle the circuit, the power usage of the photodetector needs to be calculated.

When calculating the power of the circuit in Figure 4.8, the most important elements to consider are the op-amps. As the non-inverting amplifier has high input impedance, the system can be broken down into two op-amp circuits.

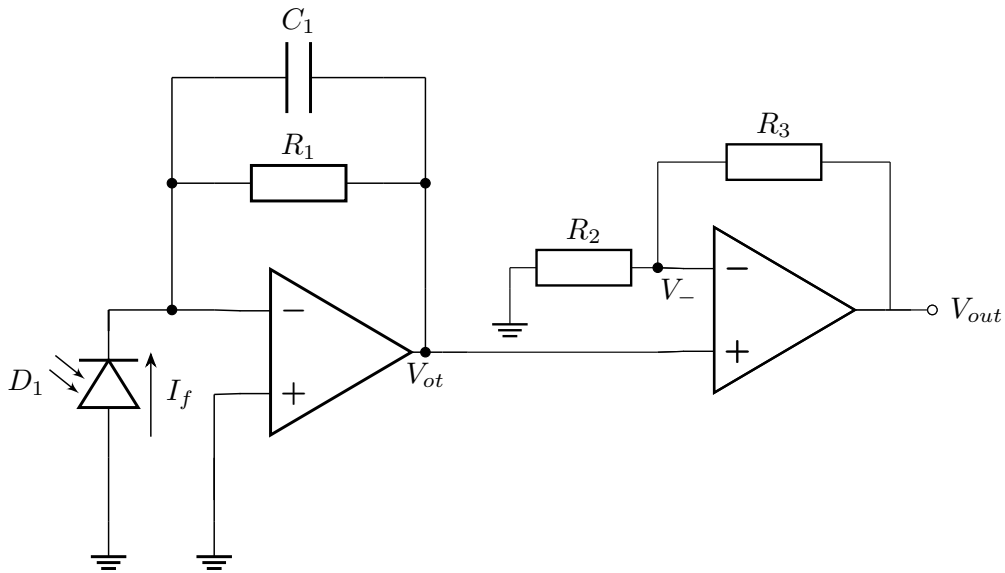


Figure 4.8: TIA with non-inverting output amplification

The op-amp in the TIA circuit has an intrinsic power dissipation caused by its quiescent current, as well as a load power dissipation. Due to the very high input impedance of the non-inverting topology that follows the TIA, there is no load current. Nevertheless, the feedback loop still draws a current  $I_{f\alpha}$  from the amplifier. Equation (4.5) shows how this current can be calculated, after which the feedback power dissipation  $I_{f\alpha}$  can be determined using Equation (4.6). It should be noted that for  $C_1R_1 \ll 1$  the equivalent impedance  $Z_1$  is equivalent to the resistance  $R_1$  at low frequencies.

$$\begin{cases} I_{f\alpha} = \frac{V_{ot}}{Z_1} \\ Z_1 = R_1 \parallel \left( \frac{1}{sC_1} \right) = \frac{R_1}{1+sC_1R_1} \end{cases} \quad (4.5)$$

$$P_{f\alpha} = (V_{cc} - V_{ot})I_{f\alpha} \quad (4.6)$$

As a characteristic of the amplifier **Integrated Circuit (IC)**, the quiescent current  $I_{q\alpha}$  can be taken from the datasheet to calculate its power dissipation  $P_{q\alpha}$  with the formula shown in Equation (4.7).

$$P_{q\alpha} = (V_{cc} - V_{ee})I_{q\alpha} \quad (4.7)$$

Ultimately, the total power dissipation  $P_\alpha$  of the TIA can be calculated by summing the results of the previous equations (see Equation (4.8)).

$$P_\alpha = P_{f\alpha} + P_{q\alpha} \quad (4.8)$$

Similarly to the amplifier that was just discussed, the non-inverting op-amp has a quiescent power dissipation  $P_{q\beta}$  and a load power dissipation  $P_{f\beta}$ . It should be noted that even though  $V_{out}$  is not connected to in Figure 4.8, the output of the photodetector in the sensing setup needs to be connected to a lock-in amplifier. Even then, the load current that runs through it is imperceptibly low, which is why the power in Equations (4.9) and (4.10) is calculated in a similar way.

$$I_{f\beta} = \frac{V_{out} - V_{ot}}{R_3} \quad (4.9)$$

$$P_{f\beta} = (V_{cc} - V_{out})I_{f\beta} \quad (4.10)$$

Equation (4.11) shows the quiescent power dissipation, which again is based on the intrinsic characteristics of the op-amp and combining all powers again yields the total power dissipation  $P_\beta$  of the amplifier, shown in Equation (4.12).

$$P_{q\beta} = (V_{cc} - V_{ee})I_{q\beta} \quad (4.11)$$

$$P_\beta = P_{f\beta} + P_{q\beta} \quad (4.12)$$

Additionally, the power dissipated by  $R_2$  is given in Equation (4.13).

$$P_2 = V_{ot} I_{f\beta} \quad (4.13)$$

## 4.6 Lock-in amplification

As a means of retrieving data, lock-in amplification is the most suitable for the setup due to its relatively low cost, signal retrieval capabilities and the possibility of using one amplifier for several setups.

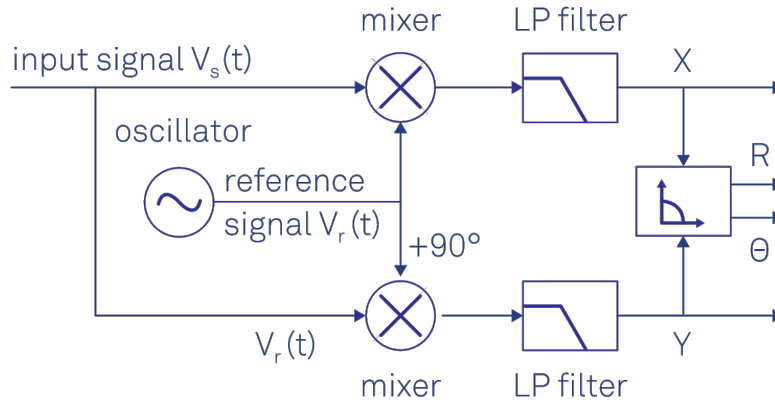


Figure 4.9: High-level diagram of a lock-in amplifier (image credit to Zurich Instruments [14])

Figure 4.9 shows an overview of how lock-in amplification works. Simply put, the amplifier receives a signal  $V_s$  and extracts the data at the frequency of a reference signal  $V_r$ . To explain this more thoroughly, lock-in amplification utilizes the fact that every signal is made of periodic waves, which are equal to zero when averaged.

$$V_s = R \cos(\omega_s t + \theta) = \frac{R}{2} e^{i(\omega_s t + \theta)} + \frac{R}{2} e^{-i(\omega_s t + \theta)} \quad (4.14)$$

Equation (4.14) shows how the mathematical expression of a sine wave signal, where  $\omega_s$  is the frequency and  $\theta$  is the phase of the signal. Using the trigonometric identity  $\cos x = \frac{1}{2}(e^{ix} + e^{-ix})$ , the signal can be represented in terms of complex numbers.

$$V_r = e^{-i\omega_r t} \quad (4.15)$$

In Equation (4.15), a simplified reference signal is shown. Real applications might require more complex reference signals, but  $V_r$  is perfect for demonstrating the lock-in principle.

$$V_m = V_s V_r = \frac{R}{2} e^{i(\omega_s - \omega_r)t + \theta} + \frac{R}{2} e^{-i(\omega_s + \omega_r)t + \theta} \quad (4.16)$$

Finally, Equation (4.16) shows the product of the signal  $V_s$  and the reference  $V_r$ . In the case of  $\omega_s = \omega_r$ , there is a signal at 0 Hz and another one at  $2\omega_s$  Hz. The latter, however, should be attenuated to an undetectable level by the low-pass filters shown in Figure 4.9. This way, both the unwanted signal appearing at double the frequency and all of the noise at different frequencies is attenuated.

# Chapter 5

## Technical design

This chapter discusses the implementation and integration of the various parts of the project. Even though the main focus here is on design and simulation, implementation is also covered where necessary.

### 5.1 Current driver

As was previously discussed, the existing driver does not need any hardware changes, but there are some notable details that play a role when configuring the driver.

#### 5.1.1 Pulsing sequences

Previously,  $T_1$  and **P-ODMR** were mentioned when discussing pulsed protocols. However, due to the high-frequency instability of the Analog Discovery signals, only sequences for  $T_1$  measurements were made. Chapter 4.2.2 presented an overview of the  $T_1$  pulsing scheme.

The lock-in amplifier reference signal can easily be generated by the Waveforms software. This is not the case for the laser driver signal. Waveforms supports custom sequence programming, however the system for writing these sequences only allows for pulses, which have a duration  $\tau_{las}$  for which  $\tau_{las} \geq \frac{T_{seq}}{100}$  holds true<sup>1</sup>. It should also be noted that using the built-in pulse generation functionalities only allow for pulses that fit the formula  $\tau_{las} = x \frac{T_{seq}}{100}$ , where  $x \in \mathbb{Z}^+$  and  $x \leq 100$ . These restrictions make it impossible for pulsing sequences to be designed in Waveforms. Thankfully, the software can read files, which makes it possible to customize a sequence more.

1	0	0	1	0
---	---	---	---	---

Figure 5.1: Sequence buffer

But before delving into implementation details, the working of pulse generation in Waveforms needs to be discussed. An example of a filled Waveforms buffer, is shown Figure 5.1. A **TTL** signal can be generated using the values from it by setting the period  $T_{seq}$  of the sequence and the peak voltage  $V_{max}$ . Those two values are necessary, because the buffer contains normalized values. In the example, each element has a value of either 0 or 1, which translate to 0 or  $V_{max}$  when entered into the function generator. Furthermore, each pulse has a value of  $\tau_{las} = \frac{T_{seq}}{5}$ .

A MATLAB script (see Figure A.4 for full script) was written to generate buffer values based on the pulse duration  $\tau_{las}$ , the scaling factor  $\gamma = \frac{T_{seq}}{\tau_{las}}$  and the normalized dark time  $t_d = \frac{\tau_d}{\tau_{las0}}$ . Figure 5.2 shows a  $T_1$  sequence where  $\tau_{las} = 20$   $\mu$ s,  $T_{seq} = 30$  ms and  $\tau_d = 200$   $\mu$ s (consequently  $\gamma = 1500$  and  $t_d = 10$ ).

<sup>1</sup> $T_{seq}$  is the period of the whole sequence

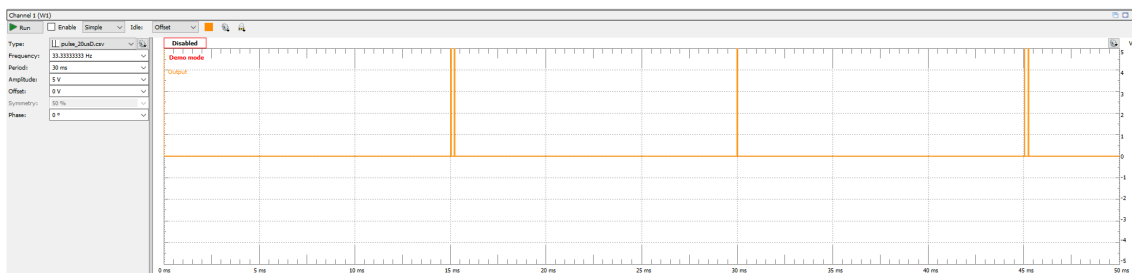


Figure 5.2: Waveforms function generator view after importing a  $T_1$  pulse sequence

## 5.2 Photodetector design

As an integral part of the sensing setup, the photodetector needs a lot of attention. Good amplification is crucial to increasing the **SNR** of the quantum setup, however the materials used need to be accessible and cheap. Based on these considerations and the design ideas presented in the functional design (see Chapter 4.5.2), the photodetection circuit can be drawn up. The first three versions presented in this section of the report address the basic requirements of a **CW-ODMR** detector, which can have a bandwidth as low as 18 Hz [15]. In contrast, the fourth iteration of the photodetector design focuses mostly on providing an increase in bandwidth, which is necessary for pulsed protocols.

### 5.2.1 First iteration

As previously mentioned, the first iteration of the PCB uses component values provided by the client. There is no specific information for the design process, aside from the fact that the original designer made the photodetector for input currents in the range of several nanoamperes. Such low inputs require high  $R_1$  values, however increasing the resistor value results in more biasing current going to the amplifier and a more limited dynamic range [16]. Furthermore, it is entirely possible that the original design did not thoroughly consider the bandwidth needed for different protocols, as **CW-ODMR** setups do not require broad bandwidths [15]. Biasing is another concern with this photodiode setup. The configuration shown in Figures 4.7 and 5.3 has the diode in the photovoltaic mode, which is suitable for low-frequency, low-light operation. In spite of this setup being suited to **CW-ODMR**, pulsed protocols require micro to nanosecond precision

### 5.2.2 Second iteration

Due to time constraints, this iteration uses the same topology as the first one. That being said, it is still designed analytically, taking into account the general practices, but also considering more subtle factors that might hinder the performance of the system. This section uses the mathematical principles presented in [17–19] to optimize the design of the existing amplifier.

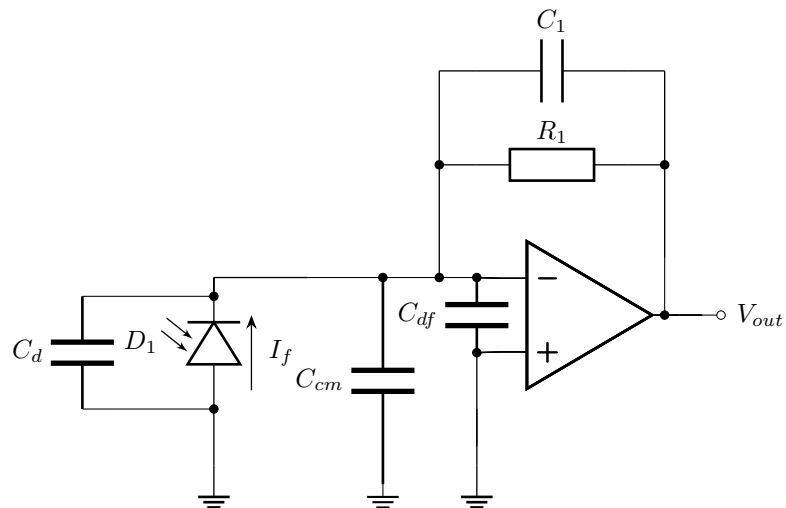


Figure 5.3: Parasitic capacitances in a **TIA** circuit

Introducing the real-world parasitic capacitances to the ideal TIA shown in Figure 4.7 results in the circuit in Figure 5.3. The diode capacitance  $C_d$ , combined with the differential and common-mode capacitances of the amplifier ( $C_{df}$  and  $C_{cm}$ ), contributes a significant amount of capacitance to the circuit and can result in instability [20].

$$C_i = C_d + C_{df} + C_{cm} \quad (5.1)$$

The combined input capacitance (Equation (5.1)) is needed when solving the equation arising from Kirchhoff's Current Law (KCL) at the inverting input of the amplifier.  $Z_1$  (Equation (5.2)), or the combined impedance of  $R_1$  and  $C_1$ , is another prerequisite for deriving the transimpedance  $Z_t$  using KCL. Additionally, the open-loop gain  $A_{ol}$  is needed for the derivation of the transimpedance. Equation (5.3) shows the open-loop gain, expressed with the Direct Current (DC) open-loop gain  $A_o$  and the open-loop cutoff frequency  $\omega_o$ , which is equivalent to  $\frac{v_{out}}{v_{in}}$ .

$$Z_1(s) = \frac{1}{\frac{1}{R_1} + sC_1} \quad (5.2)$$

$$A_{ol}(s) = A_o \frac{\omega_o}{s + \omega_o} = \frac{v_{out}}{v_{in}} \quad (5.3)$$

Finally, the values in the KCL equation (Equation (5.4)) can be substituted, from which  $Z_t$  can be derived, as seen in Equation (5.5).

$$i_f = \frac{v_i}{\frac{1}{sC_i}} + \frac{v_{in} - v_{out}}{Z_1(s)} \quad (5.4)$$

$$Z_t(s) = \frac{v_{out}}{i_f} = (R_1 \frac{A_o}{1 + A_o}) \frac{\frac{\omega_o(1+A_o)}{(C_i+C_1)R_1}}{s^2 + s \frac{1+\omega_o(C_i+(1+A_o)C_1)R_1}{(C_i+C_1)R_1} + \frac{\omega_o(1+A_o)}{(C_i+C_1)R_1}} \quad (5.5)$$

Before moving on to the pole analysis, the impact of the quality factor  $Q$  on the system response should be considered (see Equation (5.12)). Two system poles present when  $Q > 0, 5$ . For  $Q = \frac{\sqrt{3}}{3}$ , the system has a Bessel response, which has the flattest group delay, however, if  $Q = \frac{\sqrt{2}}{2}$ , then the system has a Butterworth response, which means it has the flattest possible amplitude response. Although the group delay is not as important as the amplitude response, a Bessel response also results in smaller amount of overshoot and less jitter, which is why it is preferred.

$$H(s) = H_0 \frac{(-s_1)(-s_2)}{(s - s_1)(s - s_2)} = H_0 \frac{s_1 s_2}{s^2 + s(-s_1 - s_2) + s_1 s_2} \quad (5.6)$$

Based on this consideration, the poles can be found using the general form of a second order transfer function, shown in Equation (5.6). The general form also makes it obvious that the DC gain  $H_0 \approx R_1$ , assuming that  $A_0$  is very big.

$$\begin{cases} -s_1 - s_2 = \frac{1+\omega_o(C_i+(1+A_o)C_1)R_1}{(C_i+C_1)R_1} \\ s_1 s_2 = \frac{\omega_o(1+A_o)}{(C_i+C_1)R_1} \end{cases} \quad (5.7)$$

Taking the general-equation poles and their counterparts from the  $Z_t$  expression yields the system of equations shown in Equation (5.7). Solving it results in a quadratic equation with roots shown in Equation (5.8).

$$s_{1,2} = -\frac{1 + \omega_o(C_i(1 + A_o)C_1)R_1}{2(C_i + C_1)R_1} \left( 1 \pm j \sqrt{\frac{4\omega_o(1 + A_o)(C_i + C_1)R_1}{(1 + \omega_o(C_i + (1 + A_o)C_1)R_1)^2} - 1} \right) \quad (5.8)$$

$$s_{1,2} = -\frac{3}{2} \left( 1 \pm j \frac{\sqrt{3}}{3} \right) \quad (5.9)$$

Achieving a critically-damped system, can be done by getting the roots of the general form of a Bessel filter (as seen in Equation (5.9)) and using the imaginary parts to get Equation (5.10). This expression can be solved with the quadratic formula again, finally resulting in an answer for the compensating capacitor.

$$\frac{4\omega_o(1 + A_o)(C_i + C_1)R_1}{(1 + \omega_o(C_i + (1 + A_o)C_1)R_1)^2} = \frac{4}{3} \quad (5.10)$$

$$C_1 = \frac{-2\omega_o R_1 C_i \pm \sqrt{12A_o C_i R_1 \omega_o - 3}}{2\omega_o R_1 (1 + A_o)} \quad (5.11)$$

Although Equation (5.11) says there are two solutions for the capacitor, the term under the square root will always be much bigger than the rest of the numerator<sup>2</sup>, effectively determining the sign of the roots. Simply put, this leaves only one root possible, as capacitors cannot have negative capacitance values.

To further characterize the system, the cutoff frequency  $\omega_c$  and damping factor  $Q$  can be calculated, because the system adheres to the general form, shown in Equation (5.12). Substituting in the pole expressions from Equations (5.6) and (5.7).

$$H(s) = H_o \cdot \frac{\omega_c^2}{s^2 + s \frac{\omega_c}{Q} + \omega_c^2} \quad (5.12)$$

$$\begin{cases} \omega_c = \sqrt{\frac{\omega_o(1+A_o)}{(C_i+C_1)R_1}} \\ Q = \omega_c \frac{(C_i+C_1)R_1}{1+\omega_o(C_i+(1+A_o)C_1)R_1} \end{cases} \quad (5.13)$$

In the process of designing the **TIA** circuit, the noise should be considered. Figure 5.4 shows the thermal noise generated by the resistor (modeled as the current source  $i_{nR}$ ) and the differential noise of the amplifier (modeled as the current source  $i_{nA}$ )<sup>3</sup>.

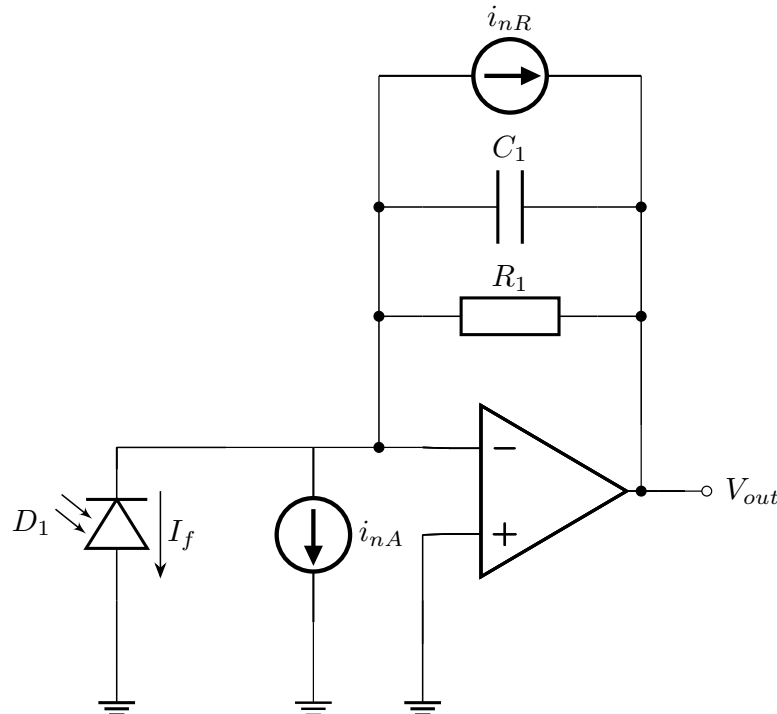


Figure 5.4: Noise sources in a **TIA** circuit

Calculating  $i_{nR}$  can be done using the Johnson-Nyquist formula, as shown in Equation (5.14). Given the fact that the temperature  $T$  and noise cutoff frequency  $\delta f$  cannot be modified in this case,  $R_1$  is the only variable that can be used to lower the thermal noise current.

$$i_{nR} = \sqrt{\frac{4kT\Delta f}{R_1}} \quad (5.14)$$

Combining the noise sources leads to Equation (5.15), which also shows that the noise can be modeled as voltage sources.

$$i_n(f) = \sqrt{i_{nR}^2 + i_{nA}^2} \Leftrightarrow v_n(f) = \sqrt{v_{nR}^2 + v_{nA}^2} \quad (5.15)$$

<sup>2</sup>Assuming real-world amplifier and diode specifications, and realistic transimpedance gain requirements

<sup>3</sup>Other noise generators, like the gate shot noise, channel noise and induced gate noise can also be calculated, but because they largely depend on the underlying technology of the **Field-Effect Transistor (FET)** op amp, they have not been investigated

In order to get a better understanding of the noise, its transfer function can be calculated in much the same way as the transimpedance (Equations 5.3 - 5.5), leading to Equation (5.16). While it might not be immediately obvious from the mathematical expression, the noise gain is 0 dB at low frequencies, but it peaks when  $f \approx f_c$ . Chapter 5.3.2 shows the noise frequency response obtained from the system equation.

$$H_n(s) = \frac{v_o}{v_n} = \frac{A_o \omega_o (s + \frac{1}{(C_i + C_1)R_1})}{s^2 + s(\frac{1}{(C_i + C_1)R_1} + \omega_o(1 + A_o \frac{C_1}{C_i + C_1})) + \frac{\omega_o(1+A_o)}{(C_i + C_1)R_1}} \quad (5.16)$$

### 5.2.3 Third iteration

While the second version of the photodetector focuses on improving the TIA performance, the third iteration is more about adapting the design for the setup. The most important considerations for the setup are function and size. Form factor constraints arise from the fact that the setup needs to be as small and adhere to the Thorlabs mounting standard. Photodetection also needs to not require many external connections or ideally be standalone. This is feasible for the data flow, as the photodetection PCB only needs light and an output to work. Unlike the data connections, version two of the design has a suboptimal power delivery system, as it uses three pins for the supply of power.

Three alternatives methods for power delivery were considered, all of which only need power and ground to work. The first one is an onboard split-rail power supply, which would take the power input and would output a fixed positive and negative voltage. Figure 5.5 shows an example of what a split-rail supply implementation might look like. There are also external option [21], which might be necessary in the future, if the setup size needs to be reduced even more.

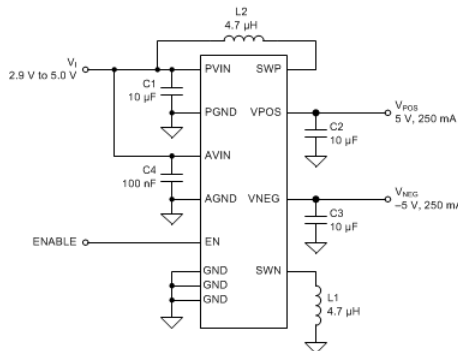


Figure 5.5: Example of a split-rail power supply implementation using the TPS65133 IC (image credit to [22])

A simpler solution would be to use a virtual ground driver IC, as it would provide a reference point at half of the supply voltage. Such a supply would also be good for decreasing the size, as the PCB needs minimal additions to satisfy the power needs of the photodetector. Additionally, a virtual ground circuit, which behaves similarly, can be made using two voltage regulators. The example in Figure 5.6 is a slightly more stable implementation

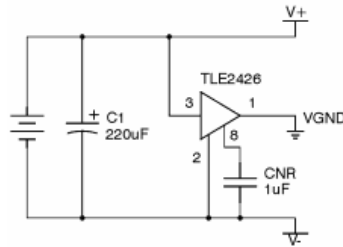


Figure 5.6: Example of a virtual ground driver using the TLE2426 IC (image credit to [23])

Another possibility is to implement a charge pump, which inverts the input voltage. This setup would only need half of the input voltage required for the virtual ground solution, effectively enabling it to be powered via a standard Universal Serial Bus (USB) connector.

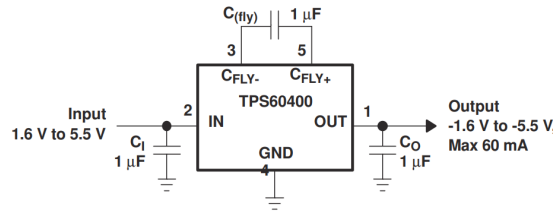


Figure 5.7: Example of a charge pump inverter using a TPS6040x family IC (image credit to [24])

	Split-rail power supply	Virtual ground	Charge pump
IC	TPS65133	TLE2426	TPS60400
$V_{in}$ (V)	5	10	5
$V_{out}$ (V)	$\pm 5$	$\pm 5$	-5
$I_{out}$ (mA)	250	40	60
Current draw ( $\mu$ A)	15	300	210

Table 5.1: Comparison of power supply options

The specifications of the different power supply solutions are shown in Table 5.1, from which can be deduced that there is a correlation between complexity and performance. The split-rail power supply, as the most complex solution, has the biggest current output range and lowest current consumption, but as illustrated in Figure 5.5, there are a number of other components that are required for proper implementation. In contrast, the virtual ground supply concept has relatively poor specifications compared to the other options, but it is the only solution that does not employ a switching mechanism, thus avoiding any possible noise. Lastly, the charge pump inverter offers reasonable performance, while not needing as many extra components as the split-rail supply. Furthermore, it addresses the stability concerns that might arise when using a virtual ground IC.

Ultimately, the charge pump is the most fit for this project, because it is relatively simple, while also offering excellent stability. The decision was reached only after taking into account the power calculations from Chapter 4.5.3, according to which all devices can handle the power requirements of the circuit. Another important factor when making the decision was the efficiency of the switching solutions. Based on slight fluctuations in the amount of current drawn, the charge pump can have as much as twice the efficiency of the split-rail power supply [22, 24], due to its high efficiency at low currents.

### 5.2.4 Fourth iteration

Although the previous iterations provided a cheap and reliable photodetector for CW-ODMR, the narrow bandwidth prevents them from measuring pulsed protocols. This iteration is specifically designed for  $T_1$  measurements.

The simplest way to increase the bandwidth of the TIA is to decrease its transimpedance gain. Additionally, an op-amp with a higher GBP (Gain-Bandwidth Product) will also contribute to a substantial increase in gain. Figure 5.8 shows the ideal version of the TIA, used in the second and third iteration of the system (in blue). It uses an AD795 amplifier, which has a 1,6 MHz Gain-Bandwidth Product. The resulting cutoff frequency is 19,69 kHz. Only swapping the AD795 for an ADA4637, which has a 79 MHz Gain-Bandwidth Product, results in the system response in orange. Its cutoff frequency is 138,87 kHz. Both lines show a system with the same transimpedance gain and consequently  $R_1$  value. On the other hand, the yellow line shows the increase in bandwidth with a 10 times smaller gain<sup>4</sup>. The ADA4637 system with 1 MΩ  $R_1$  has a cutoff frequency of 437,32 kHz.

While these changes contribute to an improved bandwidth, they are limited by the compensation capacitor  $C_1$ . Its purpose is to counteract the negative effects of the diode capacitance  $C_d$  and stabilize the frequency response of the system. In doing so, however, it also reduces the bandwidth of the system. Decreasing the capacitance of  $C_1$  outright can lead to unwanted resonance, but it is possible to stabilize  $C_d$  and consequently reduce the value of  $C_1$  by using bootstrapping. The design discussed in this section is based on [18, 25–27].

<sup>4</sup>The plot shows normalized gain of each system, which is why the first two systems (140 dB) have the same gain as the last system (120 dB)

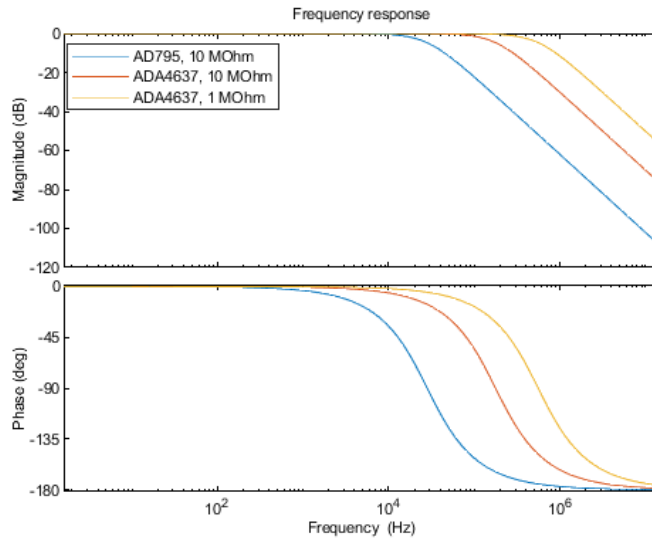


Figure 5.8: Bandwidth comparison of the third iteration of the TIA (based on AD795) and one based on an ADA4637 op-amp with a  $10\text{ M}\Omega$  and a  $1\text{ M}\Omega R_1$

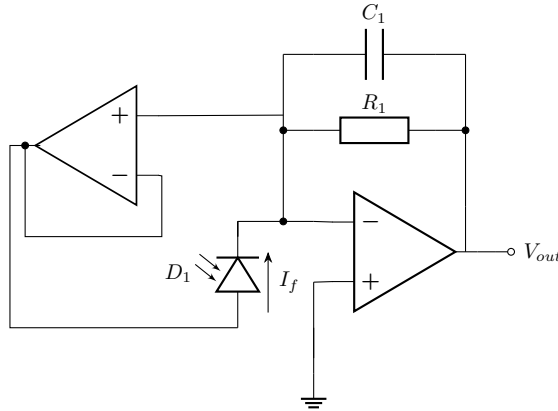


Figure 5.9: Shunt bootstrap TIA circuit

Figure 5.9 shows the bootstrapped TIA. The same analysis as in Chapter 5.2.2 can be applied to the circuit, which leads to the transimpedance  $Z_t$  in Equation (5.17). The additional op-amp buffer creates an extra pole and zero. In the expression,  $C_i$  is the sum of the common-mode and differential capacitance of the amplifier,  $C_d$  is the photodiode capacitance,  $A_o$  is the intrinsic open-loop gain of the amplifier,  $\omega_o$  is the open-loop cutoff frequency and all other parameters correspond to the ones in Figure 5.9.

$$Z_t(s) = \frac{v_{out}}{i_f} = \frac{R_1}{s^2 \frac{(C_i + C_1 + C_d)R_1}{\omega_o A_o} + s \left( \frac{(C_i + C_1 + C_d)R_1}{A_o} + C_1 R_1 + \frac{1}{\omega_o A_o} \right) - \frac{s(s + \omega_o)C_d R_1}{s + \omega_o(1 + A_o)} + \frac{A_o + 1}{A_o}} \quad (5.17)$$

Determining the ideal  $C_1$  by solving the characteristic equation of the system analytically is even harder than in the previous designs, which is why the system equation was solved by trial and error, and with the use of MATLAB to plot the system response with different capacitor values. The solution is discussed in more detail in Chapter 5.3.4.

While the improvements to the TIA are crucial for broadening its bandwidth, the changes also affect the post-amplification stage. It needs to compensate for the gain reduction that was previously discussed. Despite, a simple gain increase being a viable solution, this will also reduce the bandwidth. Similarly to the TIA, the non-inverting amplifier is also affected by the gain-bandwidth relationship, as dictated by the Gain-Bandwidth Product, shown in Equation (5.18), where  $A_v$  is the gain of the stage.

$$f_c = \frac{GBP}{A_v} \quad (5.18)$$

An alternative to increasing the gain is to add a second non-inverting stage with the same gain. By doing this, the bandwidth does not decrease as a result of the gain-bandwidth relationship, but the cutoff frequency  $f_{c\alpha}$  of single-stage non-inverting amplifier even increases as shown in Equation (5.19)<sup>5</sup> [28]. In the equation,  $A_{df}$  is the bandwidth increase due to the single-stage gain reduction.

$$f_c \approx A_{df} \left( \frac{1}{f_{c\alpha}^2} + \frac{1}{f_{c\alpha}^2} \right)^{-\frac{1}{2}} = \frac{A_{df}}{\sqrt{2}} f_{c\alpha} \quad (5.19)$$

Finally, Figure 5.10 shows the schematic of the system after all the modifications.

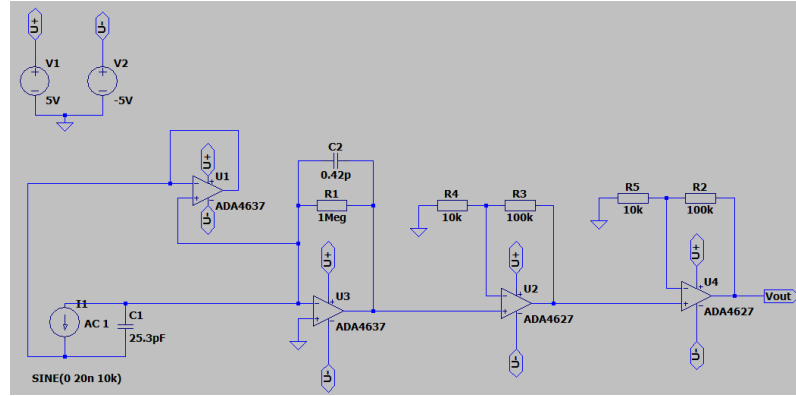


Figure 5.10: Schematic of the fourth iteration of the TIA

## 5.3 Photodetection simulation

Simulation is an important part of the designing process, as digital models of devices can be more detailed than the mathematical models presented thus far. Using different simulation programs, the real-world performance can be approximated and the math can be validated.

### 5.3.1 First iteration

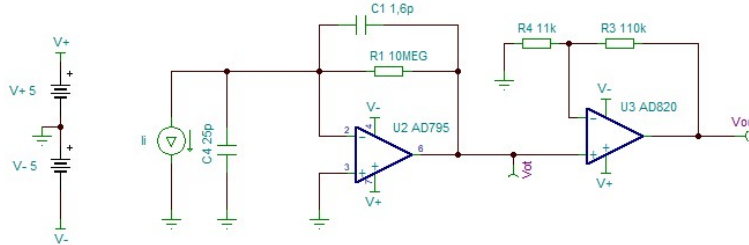


Figure 5.11: First iteration of the photodetector circuit

Figure 5.11 shows the schematic of the circuit. The capacitor  $C_4$ , as well as the current source  $I_1$  are used to simulate the behavior of a photodiode.

Tina-TI was used to simulate and visualize the DC gain and frequency response of the system, as seen in Figure 5.12. The signals  $V_{ot}$  and  $V_{out}$  correspond to the output of the transimpedance and non-inverting amplification stage respectively. The AC plot (Figure 5.12a) shows the cutoff, at 10,77 kHz, and the gain inside the gain bandwidth, which is 160,82 dB. The DC plot (Figure 5.12b) shows the voltage with respect to the current and demonstrates the linearity of the system in the range of 0 to 46,31 nA. After  $V_{out}$  reaches 5 V, the output remains fixed, because it cannot exceed the voltage provided to the amplifier.

<sup>5</sup>The formula assumes the non-inverting stages have the same parameters and use the same components as in the actual design

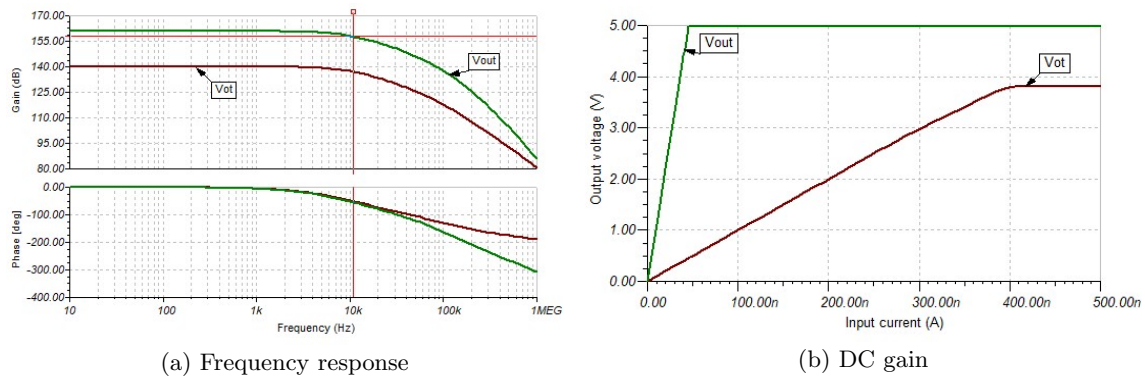


Figure 5.12: Simulation of the first iteration of the photodetector

### 5.3.2 Second iteration

A MATLAB script was written to calculate the component values based on the calculations in Chapter 5.2.2.

MATLAB calculates the component values with high precision and sourcing components with the exact values is not feasible, which is why components with standard values will be used in the setup. Simulations with standardized components were also done to compare the mathematically-ideal setup to the one in practice.

TIA version	v2 (Ideal)	v2 (Real.)	v1
$C_1$ (pF)	0,969 04	1	1,6
$f_c$ (kHz)	22,0768	21,167	11,2422
$Q$	0,577 35	0,559 96	0,354 87

Table 5.2: TIA parameters with a 10 MΩ feedback resistor  $R_1$ 

Table 5.2 contains the MATLAB calculation results and shows the values of  $f_c$  and  $Q$  when only  $C_1$  changes.  $R_1$  is kept the same, as it is equivalent the DC transimpedance  $Z_{tDC}$ <sup>6</sup>. Importantly, the results show that the previous iteration had an overdamped response. Although the quality factor with realistic component values is also lower than the ideal  $Q = \frac{\sqrt{3}}{3}$ , the system still behaves approximately like a Bessel filter.

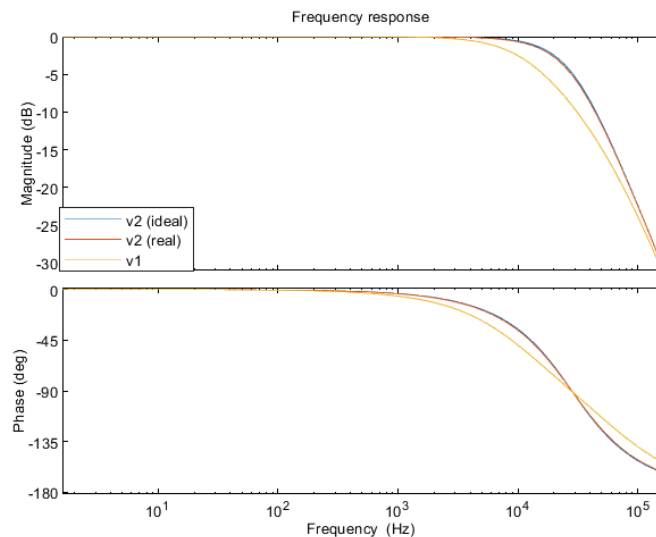


Figure 5.13: Bode plot of the system with different capacitors

Using these values, the system model was calculated and plotted in Figure 5.13. Certain

<sup>6</sup>For realistic op-amps,  $\frac{A_o}{A_o+1} \rightarrow 1$ , which means  $Z_{tDC} \equiv R_1$  can be assumed to simplify explanations

differences can be seen between the two iterations. Most notably, the cutoff frequency  $f_c$  of the first iteration is somewhat smaller than that of the second iteration. Furthermore, it can be observed that both the ideal and realistic versions of the system behave similarly.

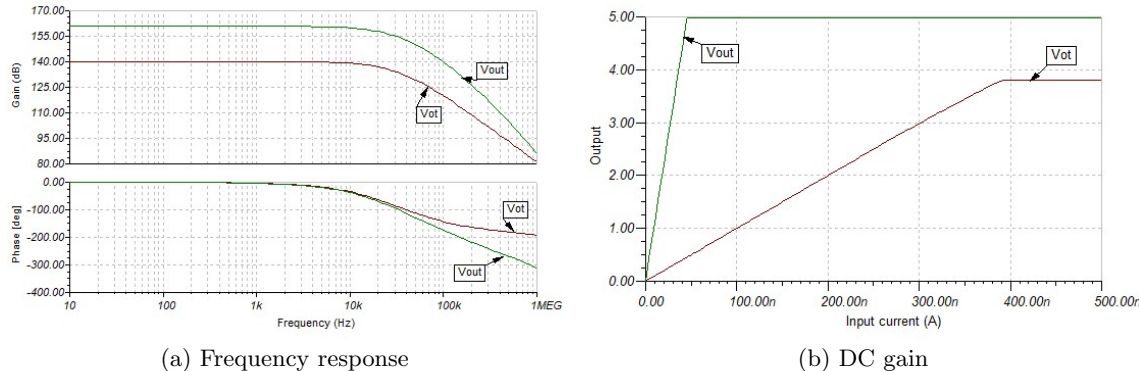


Figure 5.14: Simulation of the second iteration of the photodetector

Figure 5.14 confirms the calculations, with some slight differences that can be attributed to the **Simulation Program with Integrated Circuit Emphasis (SPICE)** models. As predicted, the frequency response of the circuit shows an increased cutoff frequency of 19,69 kHz, 8,92 kHz more than the previous iteration. Up to the cutoff frequency, the transimpedance gain is 160,83 dB, which is almost the same as the former gain of 160,82 dB. Furthermore, Figure 5.14b shows that, similarly to the first iteration, the system displays linearity in the range of 0 to 45,86 nA. This is a reduction of 450 pA compared to the previous version and also 4,14 nA less than the ideal upper limit of the linear region.

### 5.3.3 Third iteration

Before deciding on a power supply system, the power requirements needed to be compared to the specifications listed in Table 5.1. A MATLAB script, which can be found in Appendix A, was written and used to calculate that, given a  $\pm 5$  V supply, the system requires 2,3021 mA of current. All solutions can provide that amount of current with reasonable overhead, which is why the choice was based on size, complexity and stability.

### 5.3.4 Fourth iteration

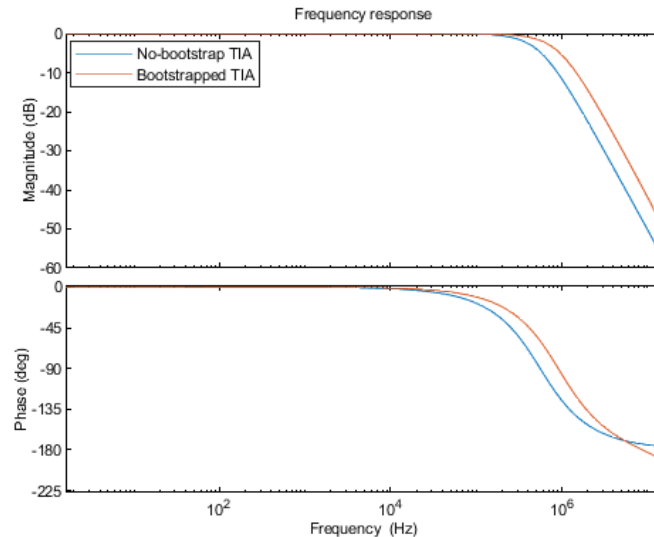


Figure 5.15: Comparison of a bootstrapped TIA and a normal TIA with the same transimpedance gain

As previously discussed, the value of the capacitor could not be determined analytically, however an approximate value was calculated using MATLAB simulations. Figure 5.15 shows that the bootstrapped system demonstrates a significantly increased bandwidth.

According to Table 5.3, the bootstrapped amplifier still has a quality factor  $Q$  close to the ideal 0,577 35, which is even better than the previous iterations of the system. Furthermore, the capacitor value is standard, meaning that the value can be used in the physical system without further approximations.

TIA version	v4 (Bootstrapped)	v4 (No bootstrap)	v2/v3
$C_1$ (pF)	0,3	0,492 65	1
$R_1$ ( $M\Omega$ )	1	1	10
$f_c$ (kHz)	724,69	437,32	21,167
$Q$	0,578 14	0,577 35	0,559 96

Table 5.3: Comparison of TIA parameters of the fourth and second/third iteration of the system

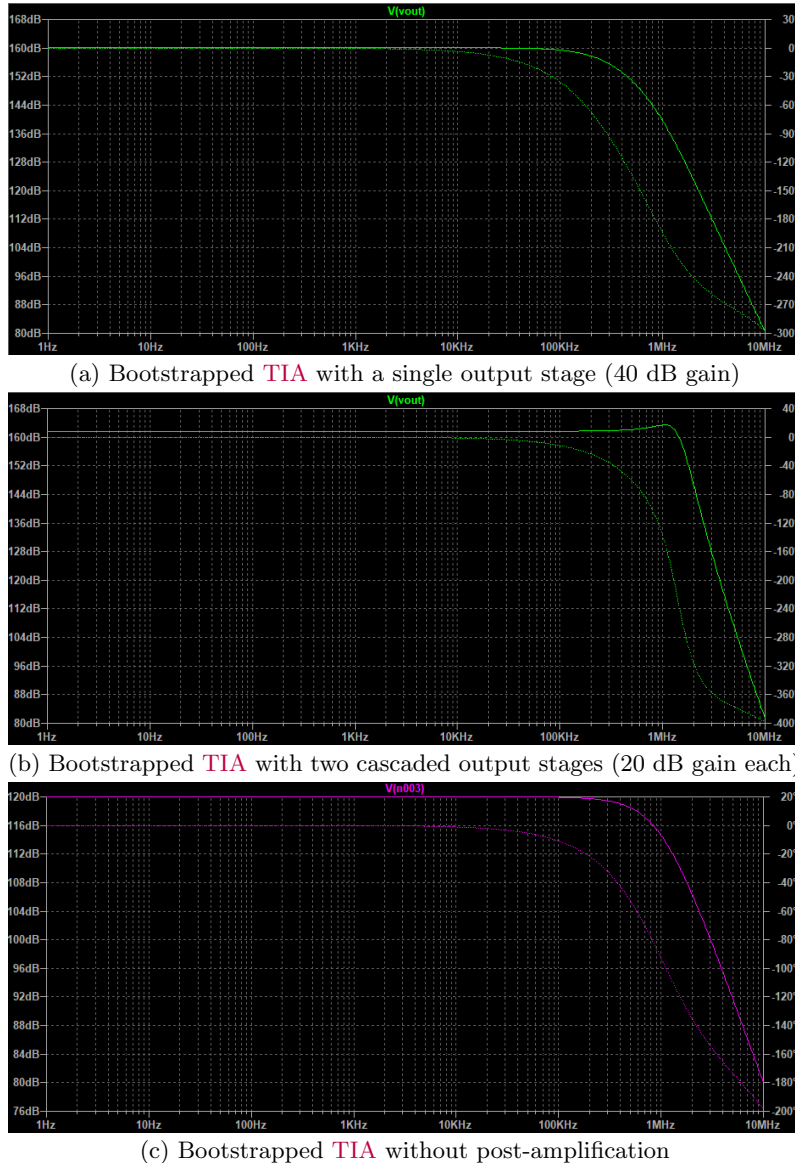


Figure 5.16: Simulation of the second iteration of the photodetector

Additionally, the post-amplification part of the system was simulated with and without the cascaded stages. Shown in Figure 5.16, the results demonstrate a significant increase in bandwidth. The plot of the bootstrapped TIA discussed in the design section (Chapter 5.2.4) with a single 40 dB non-inverting stage shows a flat response with a cutoff frequency of approximately 229 kHz. This is significantly lower than 721 kHz, which is the bandwidth of the TIA without any post-

amplification (Figure 5.16c). Figure 5.16b shows the increased bandwidth of 1,517 MHz when two stages are used instead of one. In spite of the significantly bigger cutoff frequency, the response is not maximally flat, which means the linearity at high frequencies is subpar.

## 5.4 Photodetection implementation

Creating the physical **PCB** is a more straightforward process than the design and simulation, but it still needs to be discussed.

### 5.4.1 First iteration

Figure 5.17 shows the back side of the PCB. It hosts all components, except for the photodiode, which sits unobstructed on the front side. Requirements for the physical dimensions were also set by the client. The PCB needs to fit the Thorlabs mount standard, since the rest of the setup also uses it.

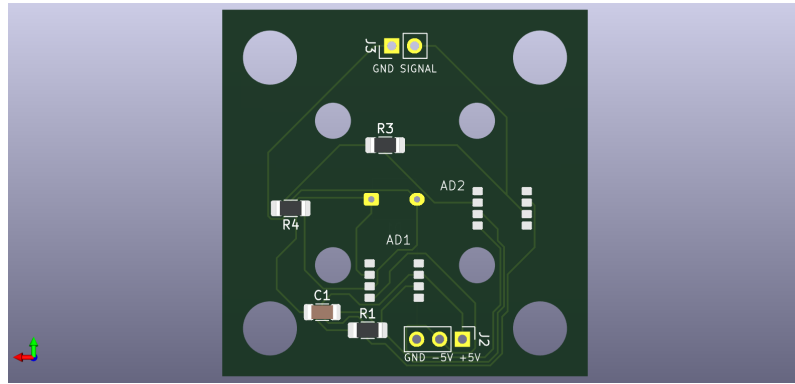


Figure 5.17: First iteration of the photodetection PCB

### 5.4.2 Second iteration

Due to the fact that the topology of the first iteration was kept, the **PCB** does not need any modifications in order to work with the circuit parameters. However, after a discussion with the client, a ground plane was added. Usually such an addition would be needed in high-speed and/or high-power use cases, but the circuit only deals with low-speed, very-low-power signals. The reason for the ground plane in the updated design is broader quantum protocol support. While **CW-ODMR** operates at low frequencies, future expansion of the sensing setup might require support for different high-speed pulsing sequences. In that case, the component values can be modified again, without the need for making a new board. Figure 5.18 shows the new board design. The updated board also has better routing than the previous version, which was done to optimize the noise performance.

### 5.4.3 Third iteration

The third version of the board has more components, which combined with the fixed board dimensions, made it more difficult to do the placing and routing. Additionally, the clearance of the power and ground nets was increased. Figure 5.19 shows the **ECAD** view of the third iteration of the photodetector.

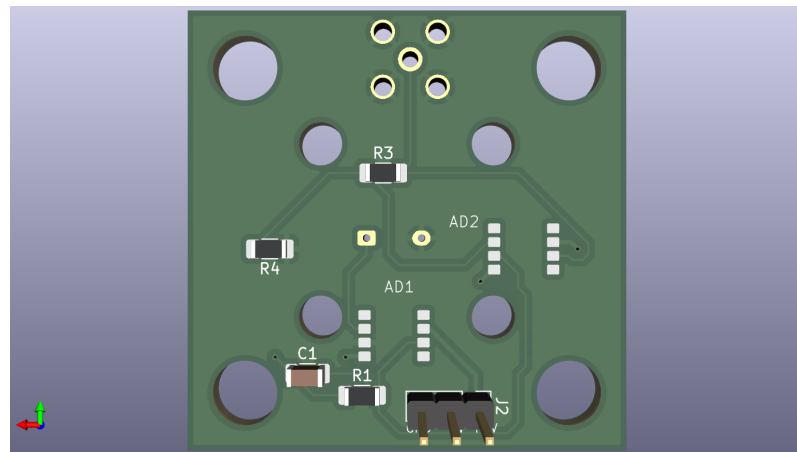


Figure 5.18: Second iteration of the photodetection PCB

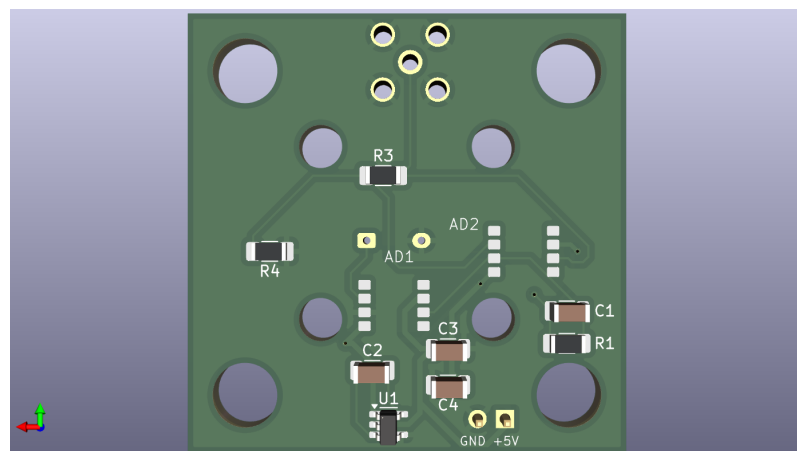


Figure 5.19: Third iteration of the photodetection PCB

# Chapter 6

## Testing and results

Table 6.1 shows all the tasks discussed in Chapter 3.4.2 and their current status. While working on the project, the client decided that purchasing a lock-in amplifier is more worthwhile than implementing OLIA, which is why tasks associated with its implementation are marked as canceled. The items with a reassigned status were given over to two students, who are also involved with the quantum sensing setup. The laser driver was reassigned, because a completely new design was needed, the making of which would require too much time. The pulse sequence script was finished and it was passed on to one of the other students for further refinement and possibly for the implementation of different protocols.

Number	Task	Status
1.1	Design photodetector	Completed
1.2	Build OLIA	Canceled
1.3	Set up laser driver	Partially completed; reassigned
2.1	Develop data acquisition software	Canceled
2.2	Program pulse sequences	Mostly completed; reassigned
3.1	Compare lock-in amplifiers	Canceled
3.2	Test quantum sensing setup	In-progress

Table 6.1: List of tasks and their completion status

### 6.1 Test goals

There are two suitable methods of characterizing the TIA. As the main point of interest is the linearity of the amplifier, the first characterization method is to simulate photodiode readings at different light intensities by modeling it as a current source. By varying the diode model current, either by sweeps or manually, the performance of the physical device can be compared to the simulations.

The second method supplements the results of the first one. It involves measuring the scattering parameters  $S_{11}$  and  $S_{21}$  and calculating the frequency response of the system. Equation (6.1) shows the formula used to approximate the transimpedance  $Z_t$  for a load resistor  $R_l$  [18]. This method provides a better overview of the transimpedance over the whole bandwidth of the photodetector.

$$Z_t(f) \approx \frac{S_{21}(f)R_l}{1 - S_{11}(f)} \quad (6.1)$$

Neither of these methods uses a real photodiode, which is why an integration test is also necessary. Using the laser driver, a square-wave signal is pulsed at different frequencies within the amplifier bandwidth. By comparing the signal output by the photodetector to the signal output by the function generator, the performance of the system can be determined.

## 6.2 Test setup

### 6.2.1 Photodiode-model characterization

Characterizing the system requires precision, due to the small currents at its input. As the diode detects ambient light and cannot be set to one current level reliably, a model needs to be used instead (see Figure 6.1). A voltage source can then be used to simulate the nanoampere photo-voltaic current  $I_f$  generated by the diode. This model assumes the parallel shunt resistance is so high that it can be omitted.

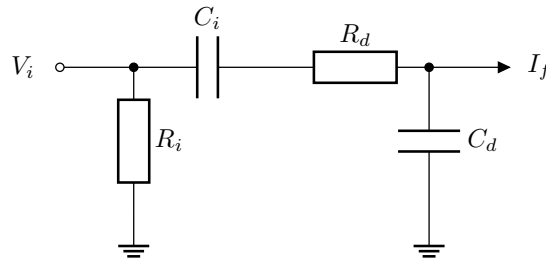


Figure 6.1: Photodiode model

Using this model, the diode current  $I_f$  can be approximated using Equation (6.2). The approximation is true only if the input impedance  $Z_i$  (see Equation (6.3)) of the TIA is significantly lower than  $R_d$  [29]. Keeping this in mind, a resistor six to seven orders of magnitude bigger was selected for the physical circuit.

$$I_f = \frac{V_i}{R_d} \quad (6.2)$$

$$Z_i = \frac{R_1}{A_o + 1} \quad (6.3)$$

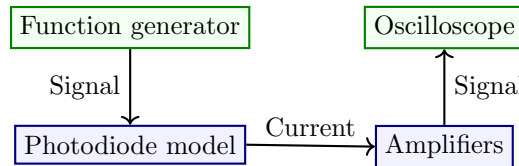


Figure 6.2: TIA characterization with photodiode model test setup

### 6.2.2 S-parameter characterization

### 6.2.3 Integration test

The integration test has a similar test setup to the complete quantum sensing setup. However, the light from the laser directly illuminates the photodiode instead of a diamond sample NV. This was done on purpose, because the bigger laser signals provide more clear information on the functioning of the photodetector. When the tests were done, the new version of the laser driver was available and its PCB included a laser, as seen in Figure 6.3. In addition to the diagram, Figure 6.4 shows what the physical measurement setup looks like.

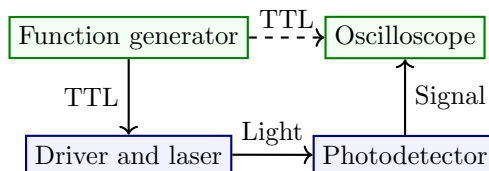


Figure 6.3: TIA integration test setup

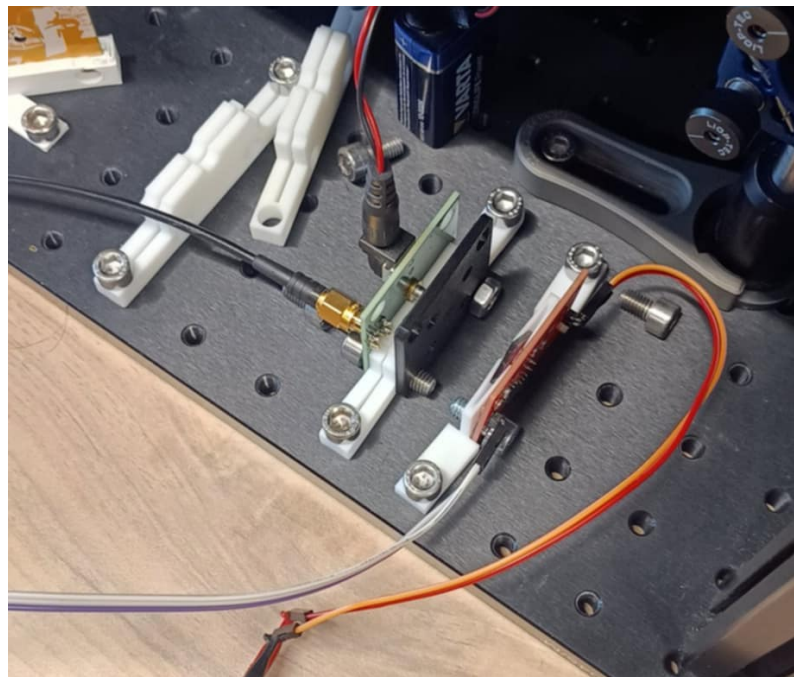


Figure 6.4: Integration test setup

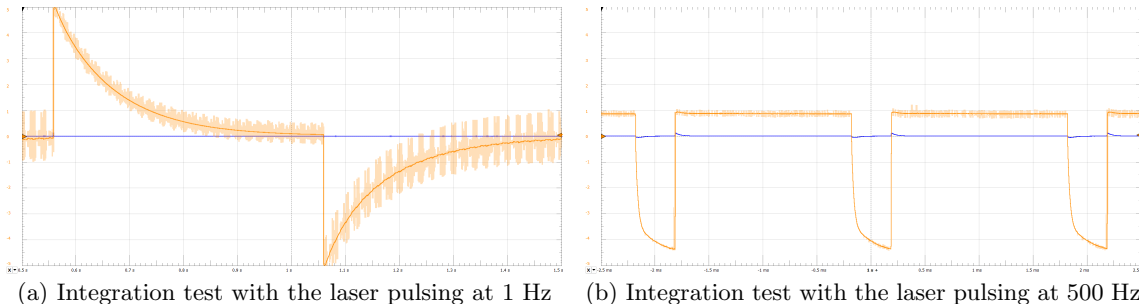
## 6.3 Results

### 6.3.1 Photodiode-model characterization

### 6.3.2 S-parameter characterization

### 6.3.3 TIA integration test

Testing with 1 and 500 Hz results in the readings shown in Figure 6.5. From the data, it can be seen that the photodetector exhibits a lower bandwidth than what was calculated for the [TIA](#). This is caused by the photovoltaic-mode diode and the high intensity of the light, which lengthen the on time and fall time of the detector.

Figure 6.5: Integration test of the first iteration of the photodetector (cutoff frequency  $f_c = 10,77$  kHz) with a focused close-proximity laser

The previous tests were done with the laser placed less than 1 cm away from the photodiode. Better measurements can be achieved by moving the laser further away and not aligning the center of the beam with the diode, both of which reduce the light intensity at the diode. This happens because overexposure in photovoltaic mode severely lengthens the rise and fall time of the photodiode, and this effect is further exacerbated by the extremely high sensitivity of the circuit. Figure 6.6 shows how the photodetector performs under the improved conditions. These measurements present a cleaner response at higher frequency, but the low-frequency measurement in Figure 6.6a demonstrates the ambient light effect on the precision of the circuit. When there is no direct laser light present, the photocurrent still generated over 200 mV of voltage. This effect is not noticeable in the higher-frequency measurements, however, they demonstrate a significant increase in signal fall time.

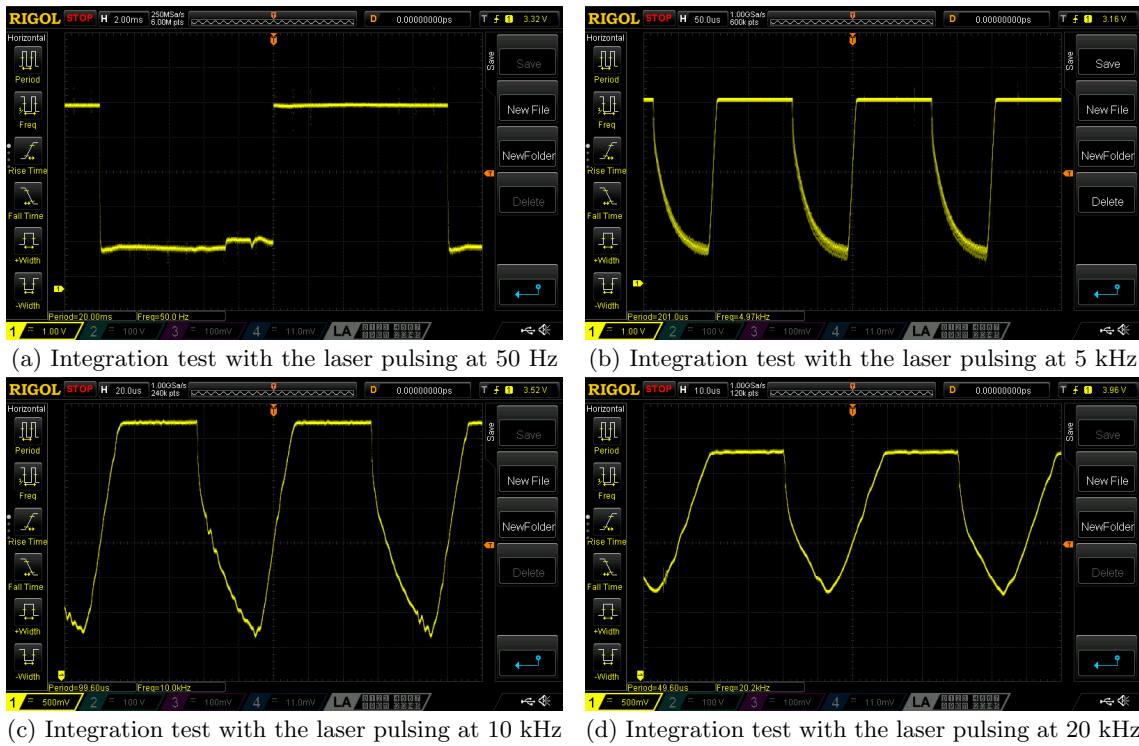


Figure 6.6: Integration test of the first iteration of the photodetector (cutoff frequency  $f_c = 10,77$  kHz) with an unfocused medium-distance laser

## 6.4 Discussion

As a result of the tests, the first iteration of the photodetector can be used for **CW-ODMR** measurements. The protocol can be executed with extremely low bandwidth photodetectors (e.g. 18 Hz [15]). That being said, pulsed protocols cannot be achieved with the first iteration of the circuit due to their high frequency requirements.

## 6.5 Known limitations

There are many factors that affect the measurements, but perhaps most prominent are the environmental lighting sources. This includes ambient sunlight, which gets through the blinds of the lab, and reflections from the laser. Both significantly affect the photodetector, especially when there is no focused light present. Reflections, in particular, also contributed to the long falling edges in the integration tests.

Furthermore, the light source in the medium-distance integration tests had to be manually adjusted, meaning that the output signals do not represent the ideal performance. To achieve ideal readings, the laser would have to be affixed and the orientation adjusted, while the intensity at the given distance is measured.

## Chapter 7

# Conclusion

In conclusion, the goal of the project, to enable detection of light signals for quantum sensing, was achieved. While there is still work to be done in order to achieve pulsed quantum protocols, the photodetector platform can be used as a reference for future designs.

According to the introduction in Chapter 3, the main purpose of the project was create a photodetector, but integration of the sensing setup was also important. Both were tackled during this project, with the focus being on photodetection. While setup integration also holds importance for the research group, most of the tasks related to it were redistributed among other students. Further refinements to the photodetector and the setup as a whole are possible. Some of the most promising ones are discussed in the recommendations in Chapter 8. Complete integration of the whole setup necessitates more work, but is achievable in the near future.

## Chapter 8

# Recommendations

There are several recommendations that are important for future implementations, as they may contribute to the precision, noise-suppression and stability of the photodetector and the quantum sensing setup as a whole.

Firstly, increasing the bandwidth is the most important future addition. To do that, the amplifier configuration needs to be changed completely. The alternative would be to significantly decrease the transimpedance gain of the [TIA](#), while increasing the gain of the non-inverting amplifier. This will introduce more noise earlier in the system, which will be amplified by the rest of the circuitry, resulting in a significant output noise increase.

Secondly, exploring avalanche photodiodes as an alternative to the p-i-n diodes currently in use, might contribute to better measurements. Although they are widely used in low-intensity applications, avalanche diodes are quite expensive. The client wanted to keep the cost low for this project, but in the future more precise pulsed protocol measurements might benefit from the internal amplification and increased precision that are offered by avalanche photodiodes.

## Appendix A

### Code

```

1 % requirements
2 V_o_tia = .5; % out voltage of tia
3 V_o = 5; % out voltage of non-inverting amp
4
5 % OPA795 specs
6 GBW = 1.5*10^6;
7 A_o_dB = 100; % DC open-loop gain in dB
8 A_o = 10^(A_o_dB/20); % DC open-loop gain
9 f_o = GBW/A_o; % open-loop cutoff frequency
10
11 % BPW34 specs
12 I_f = 50*10^-9; % max current from diode
13 C_d = 25*10^-12; % diode capacitance
14
15 % parasitic capacitances
16 C_cm = 2.2*10^-12; % common-mode capacitance
17 C_df = 2*10^-12; % differential capacitance
18 C_i = C_d + C_cm + C_df; % total parasitic capacitance
19
20 % R1 calculations
21 gain = V_o_tia/I_f;
22 gain_db = 20*log10(gain); % uncomment if you need gain in dB
23 R_1 = gain*(1 + A_o)/A_o;
24 %R_1 = 10e6; % realistic value for BPW34
25
26 % C1 calculation
27 omega_o = 2*pi*f_o;
28 C_1_num = -2*omega_o*R_1*C_i + 1 + sqrt(12*A_o*C_i*R_1*omega_o - 3)
29 ;
30 C_1_den = 2*omega_o*R_1*(1 + A_o);
31 C_1 = C_1_num/C_1_den;
32
33 % system transfer function
34 divisor = (C_i + C_1)*R_1; % normalization coefficient
35 num = A_o*omega_o/divisor; % numerator
36 s1 = (1 + omega_o*R_1*(C_i + (1 + A_o)*C_1))/divisor; % first-order
37 s
38 s0 = omega_o*(1 + A_o)/divisor; % zero-order s
39 den = [1, s1, s0];
40 tia = tf(num, den);
41 Q = sqrt(s0)/s1;
42
43 % cutoff calculations
44 omega_c = bandwidth(tia);
45 f_c = omega_c/(2*pi);
46
47 % noise transfer function
48 num = A_o*omega_o*[1 1/divisor];
49 s1 = 1/divisor + omega_o*(1 + A_o*C_1*(C_1 + C_i));
50 s0 = omega_o*(1 + A_o)/divisor; % 0th order term remains the same
51 den = [1 s1 s0];
52 tia_noise = tf(num, den);
53 tia_noisel = tia_noise;

```

Figure A.1: TIA calculations

```

1 % results and plots
2 disp('Component values')
3 disp('R1: ' + R_1/10^6 + ' MΩm')
4 disp('C1: ' + C_1*10^12 + ' pF')
5 disp('System characteristics')
6 disp('fc = ' + f_c/10^3 + ' kHz = ' + omega_c/10^3 + ' krad/s')
7 disp('Q (actual): ' + Q)
8 disp('Q (ideal) : ' + 1/sqrt(3) + ' = sqrt(3)/3')
9 % bode plot system
10 figure
11 opts = bodeoptions;
12 opts.FreqUnits = 'Hz';
13 opts.Title.String = 'Frequency response';
14 bodeplot(tia, {10, 10^6}, opts);
15 % impulse plot system
16 figure
17 ip = impulseplot(tia);
18 % bode plot noise
19 figure
20 opts_n = bodeoptions;
21 opts_n.FreqUnits = 'Hz';
22 opts_n.Title.String = 'Noise frequency response';
23 bodeplot(tia_noise, {10, 10^6}, opts_n);
24 grid on

```

Figure A.2: Plots of the TIA calculations

```

1 % values from the TIA calculation script
2 R_1 = 10e6; % transimpedance (DC component)
3 V_o_tia = .5; % out voltage of tia
4 V_o = 5; % out voltage of non-inverting amp
5
6 V_cc = 5; % positive rail
7 V_ee = -5; % negative rail
8 I_q_a = 1.5e-3; % maximum quiescent current of AD795
9 I_q_b = 0.8e-3; % maximum quiescent current of AD820
10 R_2 = 11e3; % see report
11 R_3 = 110e3; % see report
12
13 % TIA-stage power
14 I_f_a = V_o_tia/R_1;
15 P_l_a = (V_cc - V_o_tia)*I_f_a; % load power
16 P_q_a = (V_cc - V_ee)*I_q_a; % quiescent power
17 P_a = P_l_a + P_q_a; % total power
18
19 % NIA-stage power
20 I_f_b = (V_o - V_o_tia)/R_3;
21 P_l_b = (V_cc - V_o)*I_f_b; % load power
22 P_q_b = (V_cc - V_ee)*I_q_b; % quiescent power
23 P_b = P_l_b + P_q_b; % total power
24
25 % R2 power
26 P_R2 = V_o_tia*I_f_b;
27
28 % total power
29 P = P_a + P_b + P_R2;
30 I = P/(V_cc - V_ee);
31 disp('TIA power : ' + P_a*10^3 + ' mW')
32 disp('NIA power : ' + P_b*10^3 + ' mW')
33 disp('R2 power : ' + P_R2*10^3 + ' mW')
34 disp('Total power : ' + P*10^3 + ' mW')
35 disp('Supply current: ' + I*10^3 + ' mA')

```

Figure A.3: Power calculation

```

1 tp = 20e-6; % pulse duration
2 scaling_f = 1500;
3 td = 10; % normalized dark time
4 T = scaling_f * tp; % period
5 t = 1:scaling_f;
6 y = zeros(1, length(t));
7 y(1) = 1; % init pulse cancel
8 y(scaling_f/2 + 1) = 1; % init pulse
9 y(scaling_f/2 + td + 1) = 1; % readout pulse
10 plot(t, y)
11 writematrix(y, 'pulse_20usD.csv')
12 disp('Pulse duration : ' + tp*10^6 + ' us')
13 disp('Dark time : ' + td*10^6*tp + ' us')
14 disp('Sequence period : ' + T*10^3 + ' ms')

```

Figure A.4: Power calculation

# Glossary

**DC** Direct Current 20, 26

**ECAD** Electronic Computer-Aided Design 6, 29

**FET** Field-Effect Transistor 21

**Gain-Bandwidth Product** GBP 23, 24

**GUI** Graphical User Interface 6

**IC** Integrated Circuit 16, 22, 23

**KCL** Kirchhoff's Current Law 20

**MRI** Magnetic Resonance Imaging 11

**MW** Microwave 5, 6

**NV** Nitrogen Vacancy 5, 8, 10–12, 14, 32

**ODMR** Optically Detected Magnetic Resonance 4, 5, 41

**CW-ODMR** Constant-Wave ODMR 4–6, 11–13, 19, 23, 29, 34

**P-ODMR** Pulsed ODMR 5, 11, 13, 18

**OLIA** Open Lock-In Amplifier 6–8, 31

**PCB** Printed Circuit Board 7, 8, 14, 22, 29, 32

**SNR** Signal-to-Noise Ratio 7, 19

**SPICE** Simulation Program with Integrated Circuit Emphasis 27

**TIA** Transimpedance Amplifier 14–16, 19–21, 23–28, 31–33, 36

**TTL** Transistor-Transistor Logic 5, 6, 13, 14, 18

**USB** Universal Serial Bus 22

# Bibliography

- [1] Wikipedia contributors, *Nitrogen-vacancy center — Wikipedia, the free encyclopedia*, [Online; accessed 3-September-2025], 2025. [Online]. Available: [https://en.wikipedia.org/w/index.php?title=Nitrogen-vacancy\\_center&oldid=1301369588](https://en.wikipedia.org/w/index.php?title=Nitrogen-vacancy_center&oldid=1301369588).
- [2] Wikipedia contributors, *Photoluminescence — Wikipedia, the free encyclopedia*, <https://en.wikipedia.org/w/index.php?title=Photoluminescence&oldid=1309081879>, [Online; accessed 4-September-2025], 2025.
- [3] Wikipedia contributors, *Optically detected magnetic resonance — Wikipedia, the free encyclopedia*, [https://en.wikipedia.org/w/index.php?title=Optically\\_detected\\_magnetic\\_resonance&oldid=1301371272](https://en.wikipedia.org/w/index.php?title=Optically_detected_magnetic_resonance&oldid=1301371272), [Online; accessed 6-October-2025], 2025.
- [4] V. K. Sewani et al., “Coherent control of nv- centers in diamond in a quantum teaching lab,” *American Journal of Physics*, vol. 88, no. 12, pp. 1156–1169, 2020.
- [5] A. Haque and S. Sumaiya, “An overview on the formation and processing of nitrogen-vacancy photonic centers in diamond by ion implantation,” *Journal of Manufacturing and Materials Processing*, vol. 1, no. 1, p. 6, 2017.
- [6] A. J. Harvie and J. C. de Mello, “Olia: An open-source digital lock-in amplifier,” *Frontiers in Sensors*, vol. 4, p. 1102176, 2023.
- [7] Z. Song et al., “Enhancing fluorescence of diamond nv- centers for quantum sensing: A multi-layer optical antireflection coating,” *Diamond and Related Materials*, vol. 141, p. 110584, 2024.
- [8] S. Saijo et al., “Ac magnetic field sensing using continuous-wave optically detected magnetic resonance of nitrogen-vacancy centers in diamond,” *Applied Physics Letters*, vol. 113, no. 8, 2018.
- [9] Y. Zhang et al., “High-sensitivity dc magnetic field detection with ensemble nv centers by pulsed quantum filtering technology,” *Optics Express*, vol. 28, no. 11, pp. 16191–16201, 2020.
- [10] J. Jones, W. Howden, A. Murphy, et al., *T1 relaxation time*. [Online]. Available: <https://doi.org/10.53347/rID-25821>.
- [11] D. Sitnic, *Internship technical report: Nitrogen-vacancy center setup*, Saxion Applied Nanotechnology research group, 2024.
- [12] P. D. S. PHOTODIODE, *Photodiode characteristics and applications*.
- [13] P. Semig, *Transimpedance amplifier circuit*. [Online]. Available: <https://www.ti.com/lit/an/sboa268b/sboa268b.pdf>.
- [14] Z. Instruments, “Principles of lock-in detection and the state of the art. 2016,” *Internetadresse: https://www.zhinst.com/sites/default/files/li\_primer/zi\_whitepaper\_principles\_of\_lock-in\_detection.pdf*. Zuletzt aufgerufen am, vol. 17, 2018.
- [15] B. Acharya, “Compact integration of nv-based diamond quantum sensors using a small-size photodiode and on-board transimpedance amplifier,” Ph.D. dissertation, Wichita State University, 2025.
- [16] B. Black and G. Brisebois, *Transimpedance amplifiers for wide range photodiodes have challenging requirements*, 2021.
- [17] E. Margan, “Transimpedance amplifier analysis,” no, vol. 1, pp. 1–19, 2012.
- [18] E. Säckinger, *Analysis and design of transimpedance amplifiers for optical receivers*. John Wiley & Sons, 2017.
- [19] L. Horsthemke et al., “All optical magnetometry with nitrogen vacancy centers in diamonds,” Ph.D. dissertation, Universidad de Granada, 2025.

- [20] S. Cherian, “What you need to know about transimpedance amplifiers—part 1,” *Texas Instruments Incorporated*, 2016.
- [21] L. Clark, *Adafruit tps65131 split power supply boost converter*, 2025. [Online]. Available: <https://cdn-learn.adafruit.com/downloads/pdf/adafruit-tps65131-split-power-supply-boost-converter.pdf>.
- [22] *Tps65133 ±5-v, 250-ma dual-output power supply*, SLVSC01A, Rev. A, Texas Instruments, Jun. 2013.
- [23] TangentSoft. “Virtual ground circuits.” [Online]. Available: <https://tangentsoft.com/elec/vgrounds.html>.
- [24] T. Instruments, *Tps6040x unregulated 60-ma charge pump voltage inverter*, 2015.
- [25] C. Hoyle and A. Peyton, “Bootstrapping techniques to improve the bandwidth of transimpedance amplifiers,” in *IEE Colloquium on Analog Signal Processing (Ref. No. 1998/472)*, IET, 1998, pp. 7–1.
- [26] C. Hoyle and A. Peyton, “Shunt bootstrapping technique to improve bandwidth of transimpedance amplifiers,” *Electronics Letters*, vol. 35, no. 5, pp. 369–370, 1999.
- [27] S. Idrus, N. Ngajikin, N. Malik, and S. Aziz, “Performance analysis of bootstrap transimpedance amplifier for large windows optical wireless receiver,” in *2006 International RF and Microwave Conference*, IEEE, 2006, pp. 416–420.
- [28] *Cascading precision op amp stages for optimal ac and dc performance*, SBOA356, Texas Instruments, Aug. 2020.
- [29] B. Razavi, “The transimpedance amplifier [a circuit for all seasons],” *IEEE Solid-State Circuits Magazine*, vol. 11, no. 1, pp. 10–97, 2019.